minerals

MDPI

Article

Paleowind Directions over the Tarim Block during the Mesoproterozoic, Northwestern China

Chenlin Hu [1,2], Changcheng Han [1,2,*], Jinghui Ma [1,2,*], Li Deng [1,2] and Lingfeng Zhao [1,2]

1 Xinjiang Key Laboratory for Geodynamic Processes and Metallogenic Prognosis of the Central Asian Orogenic Belt, Xinjiang University, Urumqi 830017, China
2 School of Geology and Mining Engineering, Xinjiang University, Urumqi 830017, China
* Correspondence: hanchangcheng@xju.edu.cn (C.H.); majinghui10@163.com (J.M.)

Abstract: The Tarim Block is an ancient plate with a basement of ancient continental crust, which has been separated from the Rodinia supercontinent since the Neoproterozoic. During the Neoproterozoic, which lasted nearly 500 Myr, this block experienced significant evolutionary processes, such as proliferation, radioactive decay of elements, and gradual cooling and solidification. The investigation of Neoproterozoic paleogeography may shed light on the evolution of these geological events. In order to realize this potential, this study aimed to infer paleowind directions over the Tarim Block during each epoch of the Cryogenian–Ediacaran and to constrain the paleogeographic location of the Tarim Block. To this end, outcrop magnetic fabric data were employed to analyze the anisotropy of magnetic susceptibility within the Tarim Block. The anisotropy of magnetic susceptibility measurements yielded mean paleowind directions of 308° ± 69°, 277° ± 78°, and 256° ± 76° from the present north for the Early, Middle, and Late Cryogenian, respectively; the corresponding values for the Early and Late Ediacaran were 237° ± 77° and 254° ± 73° from the present north, respectively. Considering the rotation relationship of the Tarim Block from the Neoproterozoic to the present, the paleowind directions during the Early, Middle, and Late Cryogenian were ~55°, ~35°, and ~35° from the paleo-north, respectively. The paleowind directions during the Early and Late Ediacaran were ~35° and ~60° from paleo-north, respectively. By referring to the correspondence between the paleowind directions over the Tarim Block and trade winds in the Northern Hemisphere, this study provides evidence for the location of the Tarim Block during the Cryogenian–Ediacaran. The main contributions of this study can be summarized as follows: (1) paleowind patterns are established through the analysis of the anisotropy of magnetic susceptibility; (2) the paleogeographic location of the Tarim Block during the Cryogenian–Ediacaran is constrained; and (3) a reference for further study of the paleogeography of the Tarim Block during the Cryogenian–Ediacaran is provided.

Keywords: Tarim Basin; Cryogenian; Ediacaran; paleogeography; trade winds

check for updates

Citation: Hu, C.; Han, C.; Ma, J.; Deng, L.; Zhao, L. Paleowind Directions over the Tarim Block during the Mesoproterozoic, Northwestern China. *Minerals* **2022**, *12*, 1435. https://doi.org/10.3390/min12111435

Academic Editor: Aleksey Sadekov

Received: 20 September 2022
Accepted: 10 November 2022
Published: 12 November 2022

Publisher's Note: MDPI stays neutral with regard to jurisdictional claims in published maps and institutional affiliations.

1. Introduction

The Neoproterozoic is a vital period of time that lasted nearly 500 Myr. During this time span, the Rodinia supercontinent aggregated and broke up, and major global blocks experienced significant evolutionary processes [1–3]. The Tarim Block is an independent Paleozoic plate with a basement of ancient continental crust, which has been separated from the Rodinia supercontinent since the Neoproterozoic [4–6]. During the Precambrian, the Tarim Block experienced a series of complex evolutionary processes such as proliferation, radioactive decay of elements, and gradual cooling and solidification [7–9]. With the explosive appearance of Cambrian organisms approximately 540 Ma ago (i.e., Cambrian explosion of life), the evolution of the Earth entered a new period of active life [10–12]. This transformation event during the Precambrian–Cambrian marks an extremely pulsating and critical period. It was accompanied by a series of important and far-reaching profound processes, including the evolution of the Rodinia supercontinent to the Gondwana continent [13–15], oxidation events on the Earth [15–17], and the development of complex organisms such as multicellular eukaryotes [14,18,19]. The evolution of these geological events may be recorded in Neoproterozoic paleogeography [20–22]. Therefore, the basic geological study of the Neoproterozoic paleogeography of the Tarim Block would provide a basis for understanding the evolution history of early Earth events.

According to paleogeographic studies based on paleomagnetism, the Tarim Block was located at the mid–low latitude region (0–45°) of the Northern Hemisphere during the Cryogenian–Ediacaran, but there is no consensus for its paleogeographic location and rotation orientation [5,23–25] (Figure 1). Some scholars believe that the Tarim Block was located at about 40° N during the Cryogenian (~750 Ma) and that the northern area was adjacent to the northwest of the Australian Block (modern orientation) (Figure 1A). During the Ediacaran, the Tarim Block shifted southward to about 27° N, with a counterclockwise rotation [23] (Figure 1B). This suggests that the Tarim Block was gradually breaking away from the Australian Block, but not completely [23]. At that time, the Tarim Block was possibly located at the edge of the Rodinia supercontinent, which may explain the orogeny of the Tarim Block lagging behind the peak orogenic activity of the global Greenville Orogeny by approximately 100 Myr [23,26]. To some extent, this implies that the southern margin of the Tarim Block was on the edge of the supercontinent, while the northern margin was breaking away from the Australian Block at different degrees [6,8,23]. The Tarim Block subsequently aggregated with the Rodinia supercontinent but broke away from it later [4,7,23]. During the Ediacaran, the northern margin of the Tarim Block was located in an intracontinental rift, and the southern margin was located at the continental margin [23,27,28]. The breakup of the Rodinia supercontinent caused the small-scale supercontinent and Gondwana supercontinent to aggregate, consisting mainly of the present Africa, South America, Antarctica, Australia, and many smaller continental fragments [23,29,30].

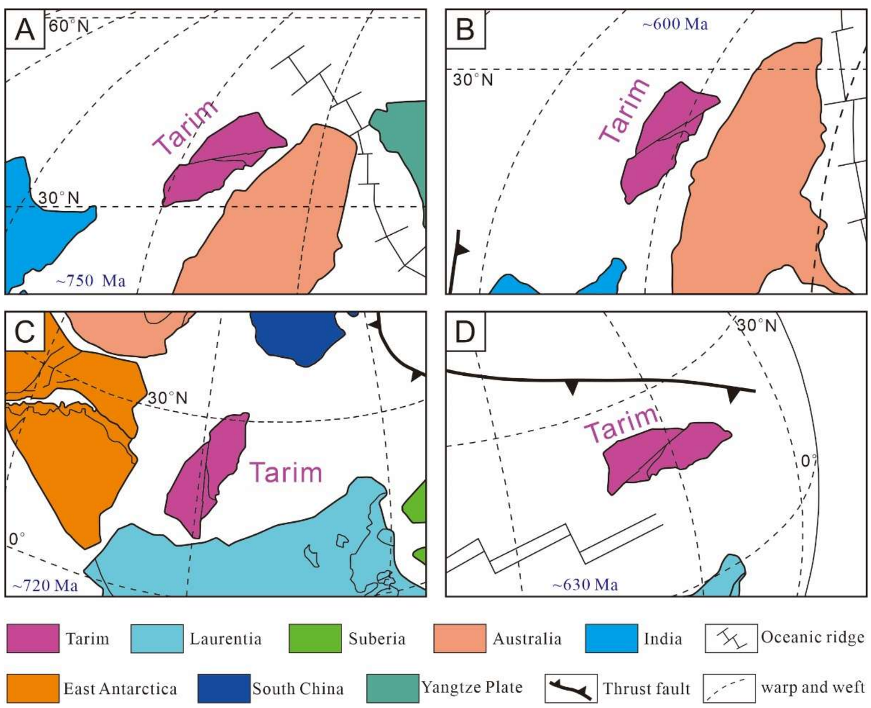

Figure 1. The Tarim Block was located at the mid–low latitude region of the Northern Hemisphere during the Cryogenian–Ediacaran. (**A**) The Tarim Block was located at about 40° N during the Cryogenian (~750 Ma), and the northern area was adjacent to the northwest of the Australian Block [23]. (**B**) The Tarim Block shifted southward to about 27° N with a counterclockwise rotation during the Ediacaran [23]. (**C**,**D**) The large-scale rotation of the Tarim Block was at near-constant paleolatitudes during the Cryogenian–Ediacaran [24].

Other scholars hold that the large-scale rotation was at near-constant paleolatitudes during the Cryogenian [24,31,32]. The rotation is coeval with the breakup of Rodinia, and the paleolatitudes of the Tarim Block agree with its placement between Australia and Laurentia, either by itself as an alternative "missing link" or joined with South China [24,31,33] (Figure 1C,D). Moreover, records of subduction-related magmatism in the Tarim Block during the Neoproterozoic suggest that the breakup of Rodinia was dynamically linked to subduction retreat along its northern margin [24,32,33]. Such a model resembles the early stages of Jurassic fragmentation within southern Gondwana and implies more complicated subduction-related dynamics of supercontinent breakup than superplume impingement alone [24,31–33]. Limited by the low accuracy of paleomagnetic methods, the paleolatitude and rotation cannot be accurately determined, leading to uncertainties in the restoration of paleowind directions. Therefore, it is necessary to quantitatively restore paleowind directions using other methods.

The present study conducted an integrated analysis of bed- to block-scale variations of the Tarim Block based on outcrop data to quantitatively reconstruct paleowind directions during the Cryogenian–Ediacaran. Paleowind directions during sedimentation were quantitatively restored through the magnetic susceptibility anisotropy analysis of samples from Precambrian strata—relatively few studies have conducted similar analyses of Precambrian strata. The objectives of this study were to (1) quantitatively reconstruct paleowind directions over the Tarim Block during the Cryogenian–Ediacaran and (2) constrain the paleogeographic location of the Tarim Block. The results of the present study can serve as a reference for applying the anisotropy of magnetic susceptibility data to the recognition of paleowind directions over Precambrian blocks.

2. Geological Setting

The Tarim Block is composed of a metamorphic basement of the Neoarchean–Neoproterozoic with overlying marine and continental sedimentary caprocks of the Cryogenian–Cenozoic [9,27,34]. During the Early Neoproterozoic, the southern and northern Tarim Block and other surrounding blocks collided and collaged to form a unified cratonic basement, which became a part of the Rodinia supercontinent [4,6,8]. The Tarim Basin is a huge polycyclic superimposed basin with a stable core position in the Tarim Block [35–37] (Figure 2A,B). The basin is a part of a land mass that broke off from the Rodinia supercontinent during the Cryogenian to Early Ediacaran. The evolution of the region to the rift stage under the stretching tectonic background during the Cryogenian marked the beginning of caprock deposition during the Neoproterozoic [4,6,34]. The Tarim Basin area was mainly dominated by depression deposition throughout the Ediacaran [38–40]. The present study focuses on the sedimentary body of the Cryogenian–Ediacaran in the Tarim Basin area (Figure 2B,C).

2.1. Tectonic Setting

During the Early Cryogenian, the Tarim Basin area entered the development period of a rift basin under the back-arc extension, developing a deep rifting and huge filling space in the center of the basin [37,41,42]. With the rapid invasion of seawater and sediment accumulation, transitional fine clastic rock deposits of shallow-coastal facies formed [8,9,41]. During the Middle to the Late Cryogenian, the subduction of the Pan-Rodinia Ocean was gradually replaced by a mantle plume under the background of the Rodinia supercontinent breakup, and the Tarim Rift Basin continued to develop with the opened South Tianshan Ocean [6,8,41]. During the Early Ediacaran, most of the space of the rift basin was filled by deposits. The deposition was dominated by terrigenous clastic deposits of silt and fine-grained sandstone, and shallow-coastal facies developed [38,39,41]. By the Late Ediacaran, the rift basin was generally filled and the carbonate tidal flats of the Shuiquan and Hangeerqiaoke formations were widely developed [38,41,43]. Under the influence of the Gaskiers glaciation, continuous moraine deposits formed in the northeast of this basin [41,44]. At this time, the rift basin was in the late developmental stage, and the large-scale coastal environment was similar to the continental sea that was globally widespread during the Early Cambrian [9,41]. The Tarim back-arc rift basin evolved from a deep sea to a shallow sea and the lithology changed from clastic rocks to carbonate rocks during the Cryogenian–Ediacaran [4,34,41] (Figure 2B,C).

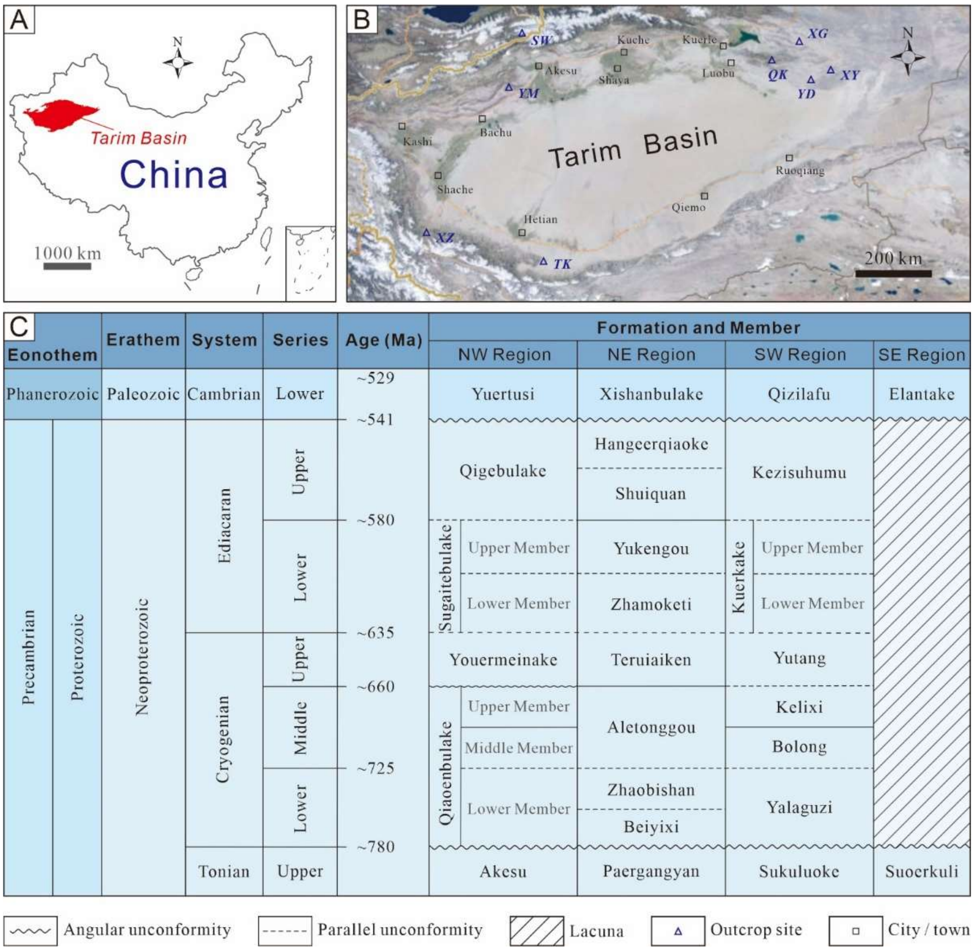

Figure 2. (**A**) Simplified map of China showing the location of the Tarim Basin (after Jiang et al. [45]). (**B**) Baidu map of the Tarim Basin showing the outcrop and drill core locations used in the present study (based on https://map.baidu.com (accessed on 17 August 2021)). Detailed information on eight outcrops (QK, SW, TK, XG, XY, XZ, YD, and YM) is given in Table S1. NW—northwestern; NE—northeastern; SW—southwestern; SE—southeastern. (**C**) Cryogenian–Ediacaran stratigraphy in the Tarim Basin (after Li et al. [46], Shi et al. [47], and Zhu et al. [48]). Geochronology from Li et al. [46], Shi et al. [47], Zhu et al. [48], and Cohen et al. [49].

2.2. Stratigraphy

Different areas of the Tarim Basin have different sedimentary characteristics, with significant differences in rock association, sedimentary structure, and strata thickness [9,34,50] (Figure 2B,C). Taking the Kuruktag area in the northeast as an example, the Cryogenian is composed of the Beiyixi, Zhaobishan, Aletonggou, and Teruiaiken formations from the bottom to top [37,50,51]. The Beiyixi Formation irregularly overlies the Tonian System with a thickness of 20–1400 m. The lower part comprises interbedding of gray thin–thick fine sandstone and siltstone, and the upper part comprises moraine with dark gray, gray-green thin–medium mudstone and silty mudstone. The Zhaobishan and Beiyixi formations have a parallel unconformity contact. The Zhaobishan Formation has a thickness of 350–1000 m, and it mainly comprises sandstone, siltstone, and mudstone deposits in a shoreland-shelf environment, with a series of small cross and hummocky beddings. The Aletongou Formation has a thickness of 90–1390 m, and it is in parallel unconformity contact with the Zhaobishan Formation. The lower part comprises massive moraines, and the upper part comprises interbeddings of gray, dark thin–medium silty mudstone in a shoreland-shelf environment and fine-grained lithic sandstone, developing a series of ripple marks. The Teruiaiken and Aletonggou formations have an integrated contact. The thickness of the Teruiaiken Formation is 500–1700 m, and it is characterized by moraine [9,34,50] (Figure 2C).

The Ediacaran is composed of the Zhamoketi, Yukengou, Shuiquan, and Hangeerqiaoke formations [34,50,52]. The Zhamoketi and Teruiaiken formations have is a parallel unconformity contact. The Zhamoketi Formation is 140–1200 m thick, and its lithology comprises micrite dolomite and limestone with a laminar structure. The Yukengou and Zhamoketi formations have a parallel unconformity contact. The Yukengou Formation is 130–760 m thick, and its lithology comprises unevenly interbedded gray-green and yellow-green siltstone and siltstone mudstone, with fine sandstone. The Shuiquan and Yukengou formations are in a conformable contact. The thickness of the Shuiquan Formation is 15–320 m. Its lower part comprises black thin–medium mudstone interbedded with gray-yellow thin-layered micrite limestone, with a striated structure. The Hangeerqiaoke Formation unconformably overlies the Shuiquan Formation. It has a thickness of 30–500 m and comprises gray and gray-green massive moraine [8,39,50]. The Tarim Block experienced regional uplift influenced by the "Keping Movement" at the end of the Ediacaran, which resulted in a regional unconformable contact between the Ediacaran and Cambrian. The strata at the top of the Ediacaran were unconformably overlain Cambrian siliceous rocks [53–55] (Figure 2C).

2.3. Depositional Environments

The Tarim Block was dominated by clastic rocks mixed with volcanic rocks and carbonate deposits during the Early Neoproterozoic and carbonate rocks during the Late Neoproterozoic [34,41,52]. This area was under deep-sea, shallow-sea, coastal, deltaic, and ice-sea transitional depositional environments: (1) The deep-sea environment mainly appeared in the Early Cryogenian due to the opening of the rift and the rapid intrusion of seawater. The environment is characterized by deposits nearly 2000 m thick. The lithology is characterized by gray-green sandstone and siltstone interlayers, interbedded with a small amount of fine gravel clastic sediments and siliceous rock, and an incomplete Bouma sequence, which belongs to a set of deep marine facies comprising a thick layer of flysch deposits. (2) In the shallow-sea environment, terrigenous detrital sediments; biogenic sediments; authigenic sediments (e.g., glauconite); and volcanic sediments, including sand, gravel, and mud, were primarily deposited. Influenced by ocean currents, tides, and storms, shallow-sea environments are conducive to the development of diverse sedimentary structure types, including cross bedding and grain sequence bedding. (3) The coastal environment occurred in the Late Ediacaran, and it is primarily characterized by carbonate rocks mixed with fine clastic deposits. Large sets of carbonate rocks occur in both the Shuiquan and Qigebulake formations. (4) The delta is an important transitional marine and continental sedimentary environment in the study area. From the ancient continent to the shallow coastal sea, it is mainly characterized by sandstone and mudstone, with plume interlacing laminations, wave marks, and sandstone lenses. (5) Ice seas are global glacial events, which are usually recorded in both land and ocean. The Kuluketag Region of the Tarim Basin developed four moraines during the Neoproterozoic, which are recorded in the Beiyixi, Aletonggou, Teruiaiken, and Hangeerqiaoke formations [34,41,52] (Figure 2B,C).

3. Sampling and Methods

3.1. Field Methods and Sample Collection

A total of eight field sites in the Tarim Basin (the Qiakemaketieshi (QK), Sawafuqi (SW), Tiekelike (TK), Xingeer (XG), Xiangyangcun (XY), Xinzanggonglu (XZ), Yaerdangshan (YD), and Youermeinake (YM) outcrops) were investigated. From these field sites, 2002 fresh samples were collected for magnetic fabric analysis (QK = 239, SW = 236, TK = 256, XG = 260, XY = 254, XZ = 255, YD = 251, and YM = 251) using a portable mini-core drill (model: D026-C) and an insertable magnetic compass. Field descriptions and abundant measurements and outcrop photos were collected at each site (Figure 2B; Table S1).

3.2. Magnetic Fabric Analysis

Each core sample had a diameter of 25 mm and was trimmed to a length of 22 mm to maintain a uniform sample volume. After preparation, each sample was measured using a magnetic susceptibility meter (model: HKB-1 (High-accuracy Kappa Bridge-1); field strength: 300 A/m; field frequency: 920 Hz; power: AC, 220 V/110 V, 50/60 Hz, and 15 W; sensitivity: 2×10^{-12} m^3) with an automated sample handling system. Each sample was measured three times along orthogonal planes.

Regarding the anisotropy of magnetic susceptibility, variations in the magnetic susceptibility field of a sample are analyzed within a three-dimensional orthogonal framework [56,57]. The anisotropy of magnetic susceptibility of a sample is typically reported as K_{max}, K_{int}, and K_{min}, representing the lengths of the maximum, intermediate, and minimum principal axes of the three-dimensional anisotropy of magnetic susceptibility ellipsoid, respectively; D-K_{max}, D-K_{int}, and D-K_{min}, representing their declinations; and I-K_{max}, I-K_{int}, and I-K_{min}, representing their inclinations. The superposition of ferromagnetic, paramagnetic, and diamagnetic grain properties yields the total anisotropy of magnetic susceptibility signals [58,59].

The quantities of K_{max}, K_{int}, and K_{min} can be combined in various ways to describe the ellipsoid shape and features of the magnetic fabric of a sample [56,60,61]. The magnetic parameters set for this purpose are as follows:

$$\text{Lineation (L)} = K_{max}/K_{int} \tag{1}$$

$$\text{Foliation (F)} = K_{int}/K_{min} \tag{2}$$

$$\text{Degree of anisotropy (P)} = K_{max}/K_{min} \tag{3}$$

$$\text{Shape factor (T)} = (2\eta 2 - \eta 1 - \eta 3)/(\eta 1 - \eta 3) \tag{4}$$

where η1, η2, and η3 are ln (K_{max}), ln (K_{int}), and ln (K_{min}), respectively.

Following the technique of [56], parameters F_{12} and F_{23}, which are used to evaluate the statistical significance of lineation and foliation, were determined from (1) epsilon ε_{12}, which is the half-angle uncertainty of K_{max} in the plane joining K_{max} and K_{int}, and (2) epsilon ε_{23}, which is the half-angle uncertainty of K_{int} in the plane joining K_{int} and K_{min}. All of the above parameters were calculated using the Safyr and Anisoft software packages [62].

4. Results

The anisotropy of magnetic susceptibility has been widely used as an indicator of paleowind or paleocurrent directions [59,63,64]. Hydrodynamic experiments have revealed the influence of wind or water motion on grain orientation [65–67]: under quiet conditions, the maximum anisotropy of magnetic susceptibility axes is randomly distributed (Figure S1A); under a strong unidirectional flow, oblate particles tend to produce an imbricated fabric in the direction of flow, and elongated particles tend to produce an imbricated fabric parallel to the direction of transport (Figure S1B); under bidirectional flow, elongated grains may be aligned perpendicular to the directions of fluid movement (Figure S1C).

Most samples collected at all locales in the present study exhibited an oblate magnetic fabric (Figures 3 and 4) [56]. The observed proportionality of the degree of anisotropy (P) to foliation (F) was consistent with a subordinate role for lineation (L) (Figure 5). These features are typical of sediments deposited by wind or water currents [56,59]. Inverse relationships are shown by ε_{12} and L (Figure 6) and by ε_{23} and F (Figure 7), which are products of increased measurement errors for weak lineations and foliations, respectively. In contrast, the absence of a correlation between ε_{12} and F suggests that the lineation and foliation subfabrics were probably determined by the orientations of different minerals (Figures 8 and 9).

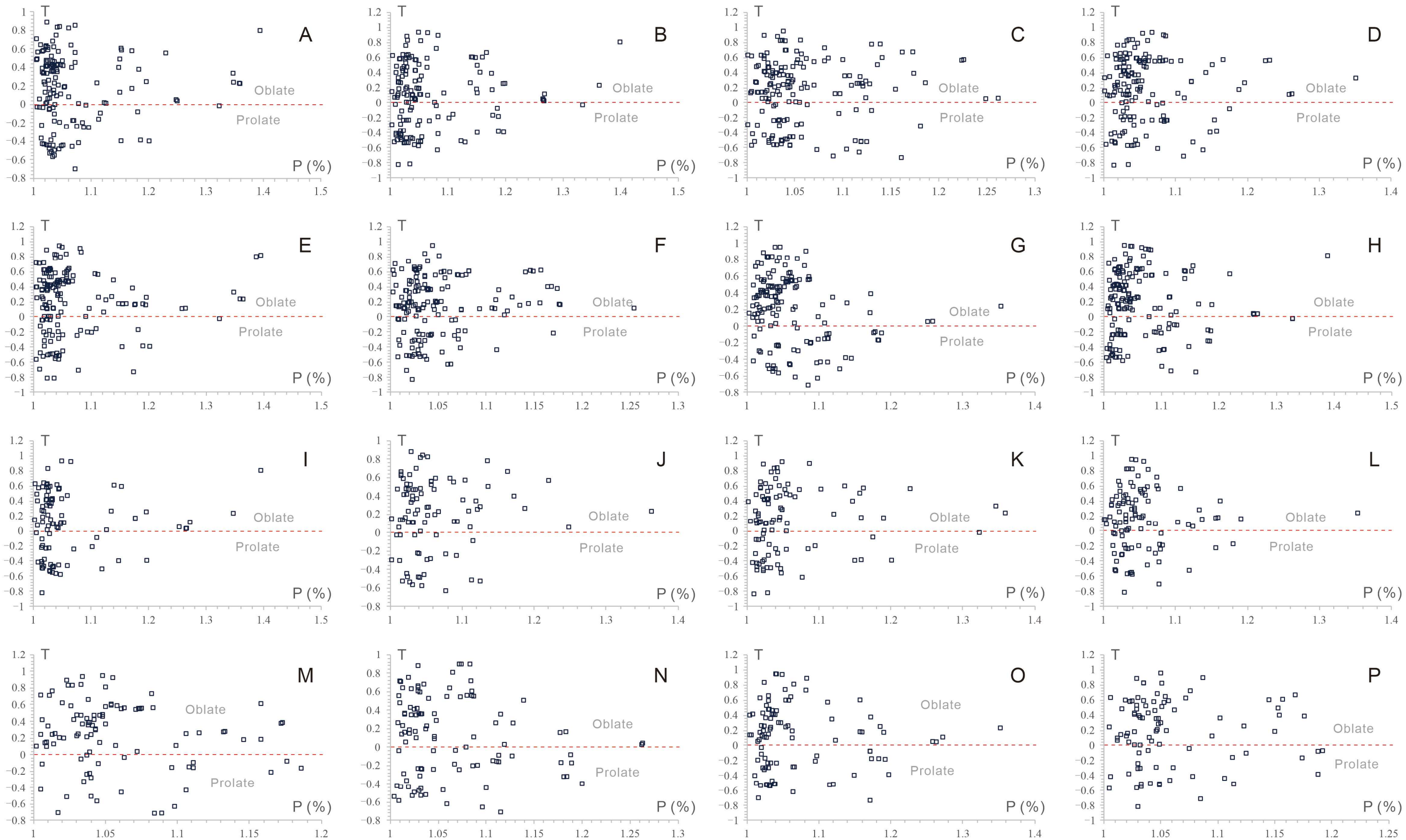

Figure 3. Relationships between the anisotropy of magnetic susceptibility parameters of P and T. (**A**) Samples from Cryogenian units at QK Outcrop (n = 145). (**B**) Samples from Cryogenian units at SW Outcrop (n = 144). (**C**) Samples from Cryogenian units at TK Outcrop (n = 158). (**D**) Samples from Cryogenian units at XG Outcrop (n = 153). (**E**) Samples from Cryogenian units at XY Outcrop (n = 155). (**F**) Samples from Cryogenian units at XZ Outcrop (n = 152). (**G**) Samples from Cryogenian units at YD Outcrop (n = 154). (**H**) Samples from Cryogenian units at YM Outcrop (n = 160). (**I**) Samples from Ediacaran units at QK Outcrop (n = 94). (**J**) Samples from Ediacaran units at SW Outcrop (n = 92). (**K**) Samples from Ediacaran units at TK Outcrop (n = 98). (**L**) Samples from Ediacaran units at XG Outcrop (n = 107). (**M**) Samples from Ediacaran units at XY Outcrop (n = 99). (**N**) Samples from Ediacaran units at XZ Outcrop (n = 103). (**O**) Samples from Ediacaran units at YD Outcrop (n = 97). (**P**) Samples from Ediacaran units at YM Outcrop (n = 91).

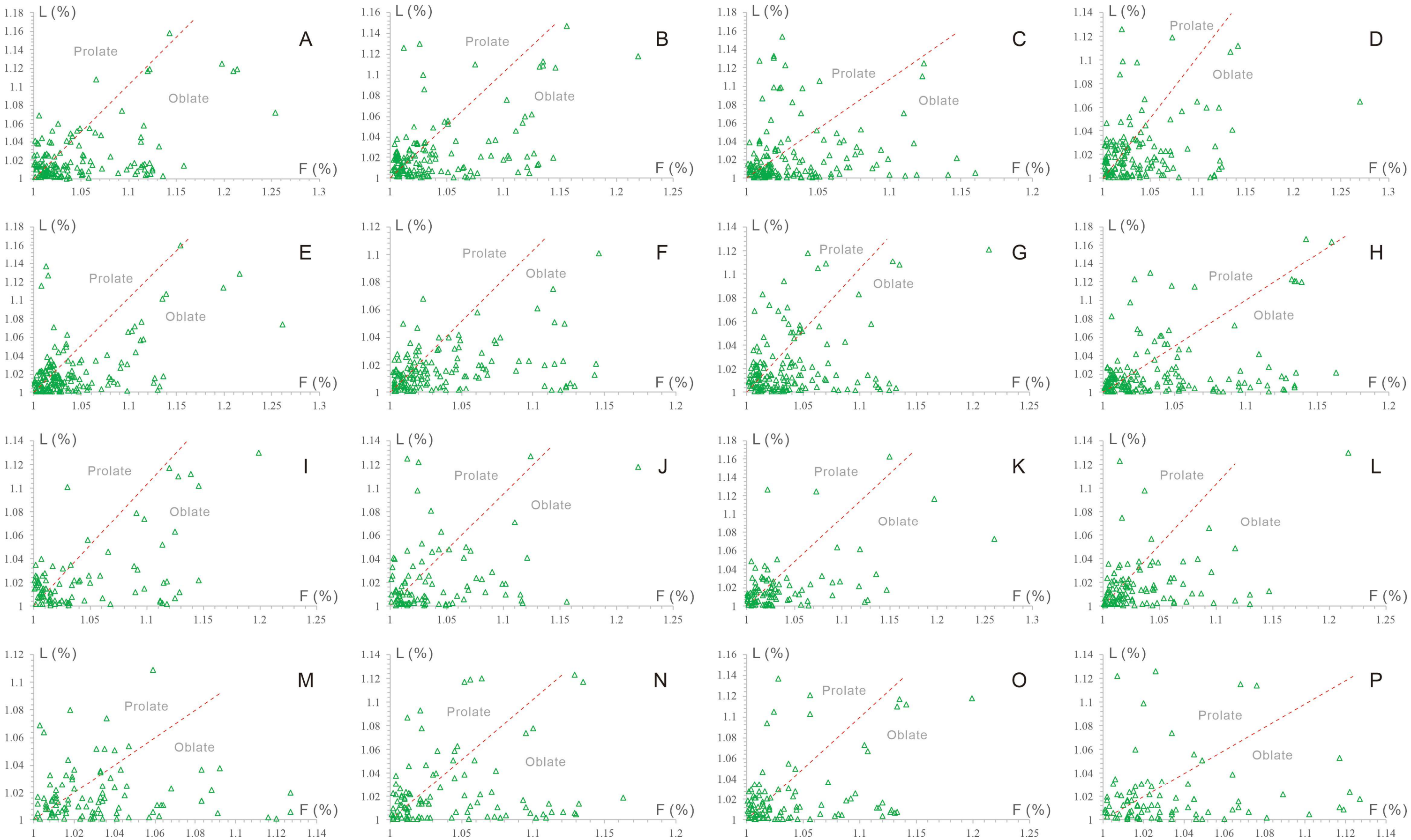

Figure 4. Relationships between the anisotropy of magnetic susceptibility parameters of F and L. (**A**) Samples from Cryogenian units at QK Outcrop (*n* = 145). (**B**) Samples from Cryogenian units at SW Outcrop (*n* = 144). (**C**) Samples from Cryogenian units at TK Outcrop (*n* = 158). (**D**) Samples from Cryogenian units at XG Outcrop (*n* = 153). (**E**) Samples from Cryogenian units at XY Outcrop (*n* = 155). (**F**) Samples from Cryogenian units at XZ Outcrop (*n* = 152). (**G**) Samples from Cryogenian units at YD Outcrop (*n* = 154). (**H**) Samples from Cryogenian units at YM Outcrop (*n* = 160). (**I**) Samples from Ediacaran units at QK Outcrop (*n* = 94). (**J**) Samples from Ediacaran units at SW Outcrop (*n* = 92). (**K**) Samples from Ediacaran units at TK Outcrop (*n* = 98). (**L**) Samples from Ediacaran units at XG Outcrop (*n* = 107). (**M**) Samples from Ediacaran units at XY Outcrop (*n* = 99). (**N**) Samples from Ediacaran units at XZ Outcrop (*n* = 103). (**O**) Samples from Ediacaran units at YD Outcrop (*n* = 97). (**P**) Samples from Ediacaran units at YM Outcrop (*n* = 91).

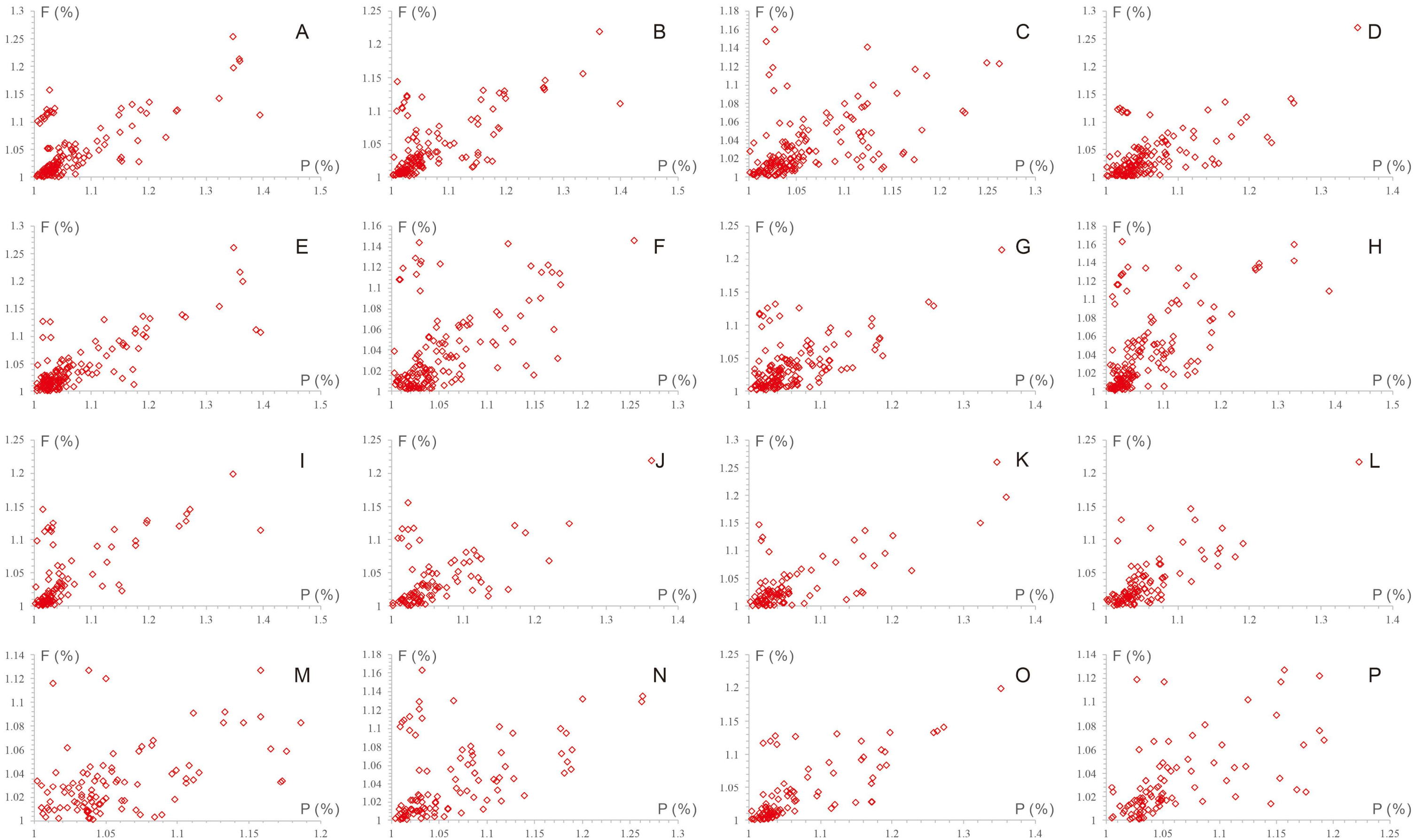

Figure 5. Relationships between the anisotropy of magnetic susceptibility parameters of P and F. (**A**) Samples from Cryogenian units at QK Outcrop (*n* = 145). (**B**) Samples from Cryogenian units at SW Outcrop (*n* = 144). (**C**) Samples from Cryogenian units at TK Outcrop (*n* = 158). (**D**) Samples from Cryogenian units at XG Outcrop (*n* = 153). (**E**) Samples from Cryogenian units at XY Outcrop (*n* = 155). (**F**) Samples from Cryogenian units at XZ Outcrop (*n* = 152). (**G**) Samples from Cryogenian units at YD Outcrop (*n* = 154). (**H**) Samples from Cryogenian units at YM Outcrop (*n* = 160). (**I**) Samples from Ediacaran units at QK Outcrop (*n* = 94). (**J**) Samples from Ediacaran units at SW Outcrop (*n* = 92). (**K**) Samples from Ediacaran units at TK Outcrop (*n* = 98). (**L**) Samples from Ediacaran units at XG Outcrop (*n* = 107). (**M**) Samples from Ediacaran units at XY Outcrop (*n* = 99). (**N**) Samples from Ediacaran units at XZ Outcrop (*n* = 103). (**O**) Samples from Ediacaran units at YD Outcrop (*n* = 97). (**P**) Samples from Ediacaran units at YM Outcrop (*n* = 91).

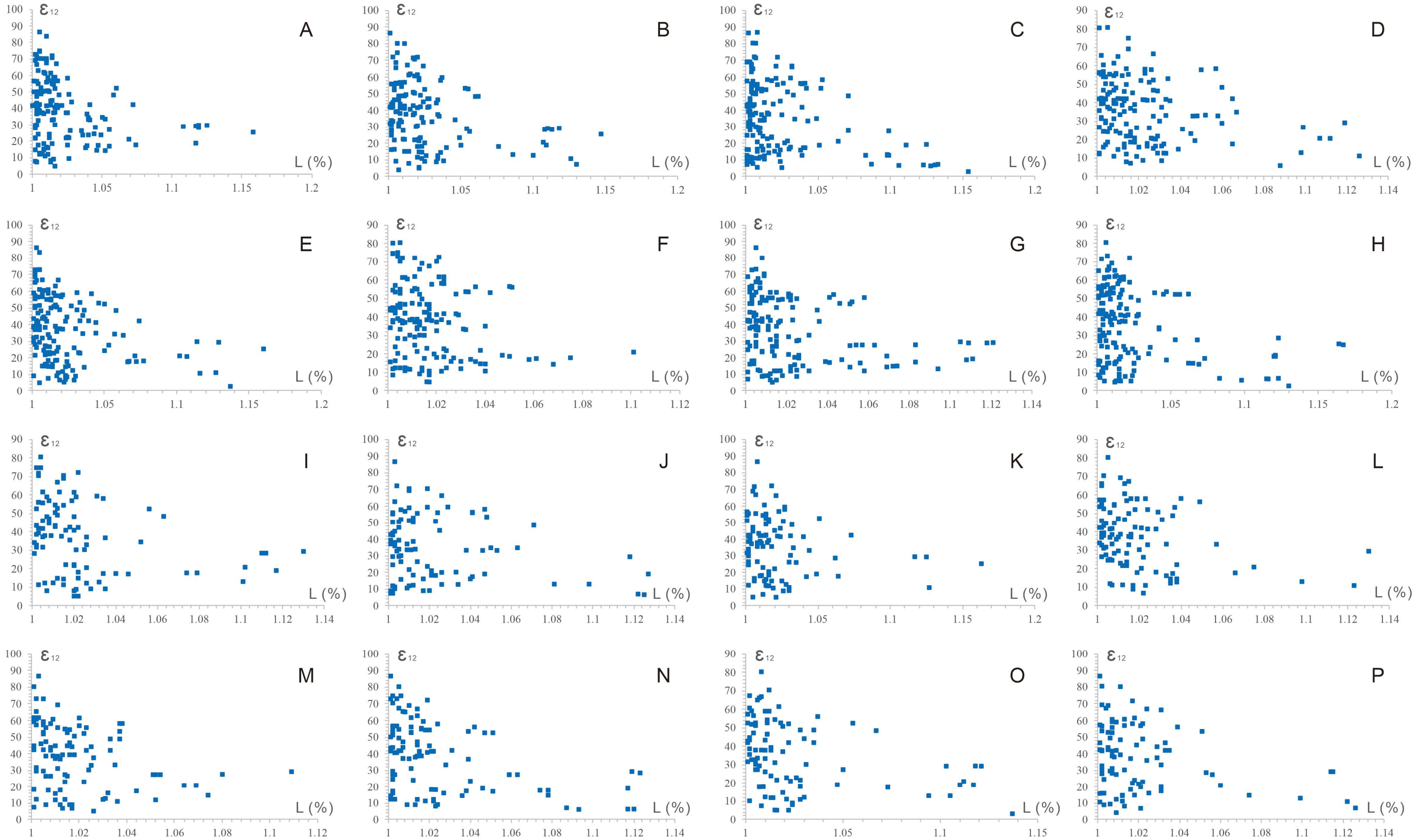

Figure 6. Relationships between the anisotropy of magnetic susceptibility parameters of L and ε_{12}. (**A**) Samples from Cryogenian units at QK Outcrop (n = 145). (**B**) Samples from Cryogenian units at SW Outcrop (n = 144). (**C**) Samples from Cryogenian units at TK Outcrop (n = 158). (**D**) Samples from Cryogenian units at XG Outcrop (n = 153). (**E**) Samples from Cryogenian units at XY Outcrop (n = 155). (**F**) Samples from Cryogenian units at XZ Outcrop (n = 152). (**G**) Samples from Cryogenian units at YD Outcrop (n = 154). (**H**) Samples from Cryogenian units at YM Outcrop (n = 160). (**I**) Samples from Ediacaran units at QK Outcrop (n = 94). (**J**) Samples from Ediacaran units at SW Outcrop (n = 92). (**K**) Samples from Ediacaran units at TK Outcrop (n = 98). (**L**) Samples from Ediacaran units at XG Outcrop (n = 107). (**M**) Samples from Ediacaran units at XY Outcrop (n = 99). (**N**) Samples from Ediacaran units at XZ Outcrop (n = 103). (**O**) Samples from Ediacaran units at YD Outcrop (n = 97). (**P**) Samples from Ediacaran units at YM Outcrop (n = 91).

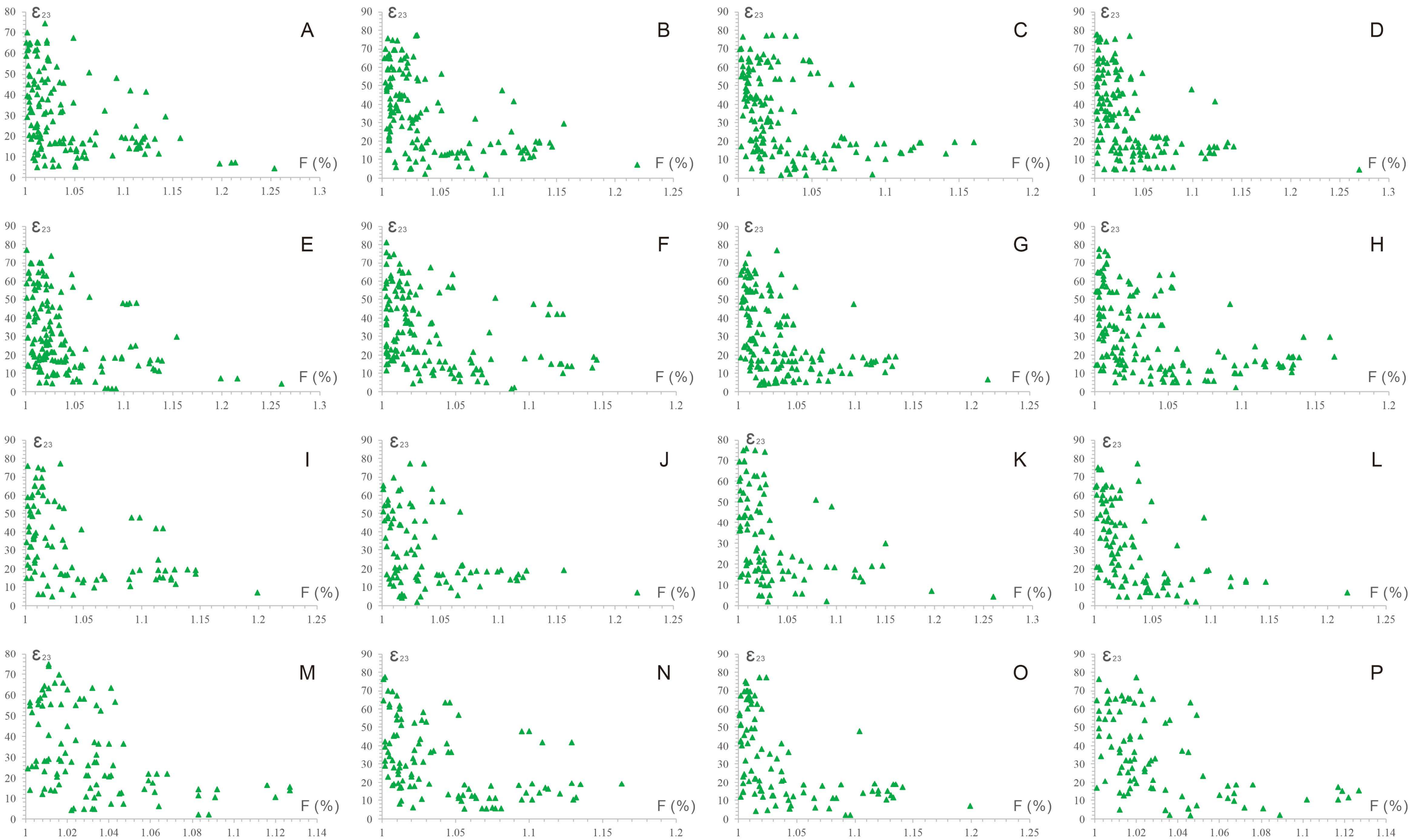

Figure 7. Relationships between the anisotropy of magnetic susceptibility parameters of F and ε_{23}. (**A**) Samples from Cryogenian units at QK Outcrop (n = 145). (**B**) Samples from Cryogenian units at SW Outcrop (n = 144). (**C**) Samples from Cryogenian units at TK Outcrop (n = 158). (**D**) Samples from Cryogenian units at XG Outcrop (n = 153). (**E**) Samples from Cryogenian units at XY Outcrop (n = 155). (**F**) Samples from Cryogenian units at XZ Outcrop (n = 152). (**G**) Samples from Cryogenian units at YD Outcrop (n = 154). (**H**) Samples from Cryogenian units at YM Outcrop (n = 160). (**I**) Samples from Ediacaran units at QK Outcrop (n = 94). (**J**) Samples from Ediacaran units at SW Outcrop (n = 92). (**K**) Samples from Ediacaran units at TK Outcrop (n = 98). (**L**) Samples from Ediacaran units at XG Outcrop (n = 107). (**M**) Samples from Ediacaran units at XY Outcrop (n = 99). (**N**) Samples from Ediacaran units at XZ Outcrop (n = 103). (**O**) Samples from Ediacaran units at YD Outcrop (n = 97). (**P**) Samples from Ediacaran units at YM Outcrop (n = 91).

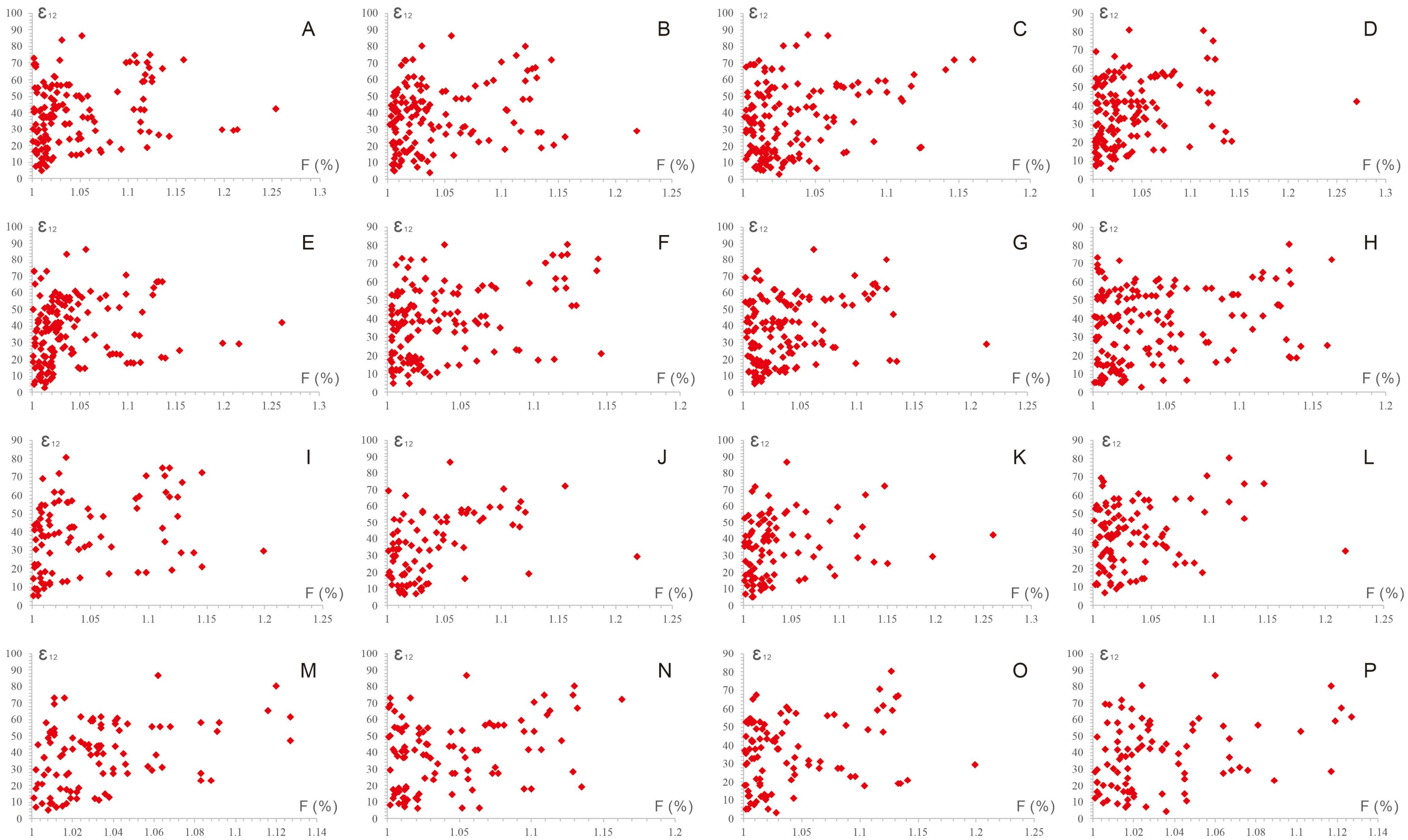

Figure 8. Relationships between the anisotropy of magnetic susceptibility parameters of F and ε_{12}. (**A**) Samples from Cryogenian units at QK Outcrop (n = 145). (**B**) Samples from Cryogenian units at SW Outcrop (n = 144). (**C**) Samples from Cryogenian units at TK Outcrop (n = 158). (**D**) Samples from Cryogenian units at XG Outcrop (n = 153). (**E**) Samples from Cryogenian units at XY Outcrop (n = 155). (**F**) Samples from Cryogenian units at XZ Outcrop (n = 152). (**G**) Samples from Cryogenian units at YD Outcrop (n = 154). (**H**) Samples from Cryogenian units at YM Outcrop (n = 160). (**I**) Samples from Ediacaran units at QK Outcrop (n = 94). (**J**) Samples from Ediacaran units at SW Outcrop (n = 92). (**K**) Samples from Ediacaran units at TK Outcrop (n = 98). (**L**) Samples from Ediacaran units at XG Outcrop (n = 107). (**M**) Samples from Ediacaran units at XY Outcrop (n = 99). (**N**) Samples from Ediacaran units at XZ Outcrop (n = 103). (**O**) Samples from Ediacaran units at YD Outcrop (n = 97). (**P**) Samples from Ediacaran units at YM Outcrop (n = 91).

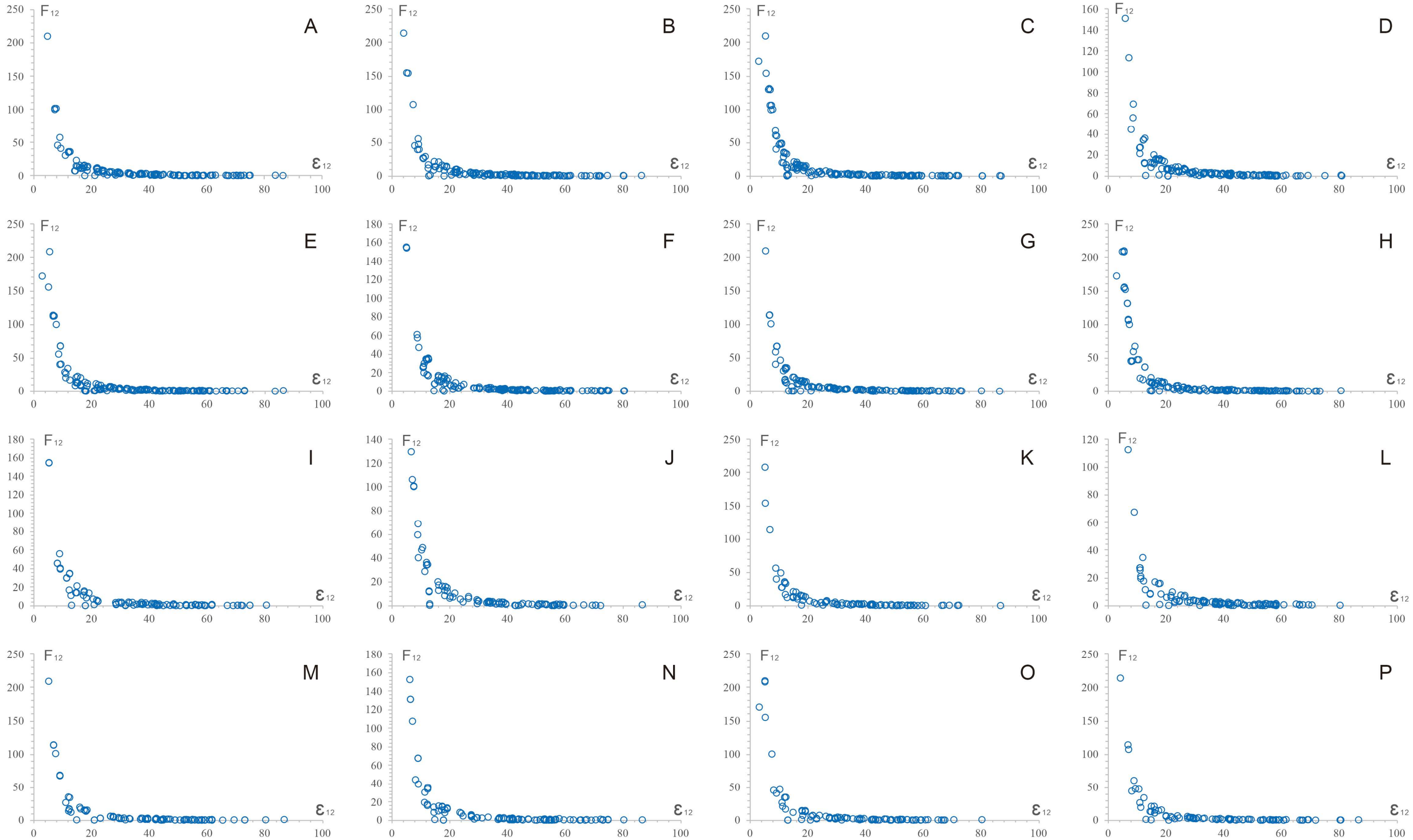

Figure 9. Relationships between the anisotropy of magnetic susceptibility parameters of ε_{12} and F_{12}. (**A**) Samples from Cryogenian units at QK Outcrop (*n* = 145). (**B**) Samples from Cryogenian units at SW Outcrop (*n* = 144). (**C**) Samples from Cryogenian units at TK Outcrop (*n* = 158). (**D**) Samples from Cryogenian units at XG Outcrop (*n* = 153). (**E**) Samples from Cryogenian units at XY Outcrop (*n* = 155). (**F**) Samples from Cryogenian units at XZ Outcrop (*n* = 152). (**G**) Samples from Cryogenian units at YD Outcrop (*n* = 154). (**H**) Samples from Cryogenian units at YM Outcrop (*n* = 160). (**I**) Samples from Ediacaran units at QK Outcrop (*n* = 94). (**J**) Samples from Ediacaran units at SW Outcrop (*n* = 92). (**K**) Samples from Ediacaran units at TK Outcrop (*n* = 98). (**L**) Samples from Ediacaran units at XG Outcrop (*n* = 107). (**M**) Samples from Ediacaran units at XY Outcrop (*n* = 99). (**N**) Samples from Ediacaran units at XZ Outcrop (*n* = 103). (**O**) Samples from Ediacaran units at YD Outcrop (*n* = 97). (**P**) Samples from Ediacaran units at YM Outcrop (*n* = 91).

The geographic orientations of the principal anisotropy of magnetic susceptibility axes were plotted on stereonets for visualization. The sample set was then screened to isolate the most significant K_{max} declination using the techniques of Lagroix and Banerjee [56] and Zhu et al. [58]. All D-K_{max} with $F_{12} < 4$ and $\varepsilon_{12} > 22.5°$ were rejected to eliminate noisy directions. The rejection of samples with $F_{12} < 4$ yielded a confidence ratio of 1.0 for the intermediate and minimum susceptibility axes of the lineation axis, and the rejection of samples with $\varepsilon_{12} > 22.5°$ yielded a confidence ratio of 1.0 for maximum and intermediate susceptibility axes in the foliation plane. I-K_{min} is another parameter used in screening the data of the anisotropy of magnetic susceptibility; I-K_{min} values > 70° generally correspond to an undisturbed (less reworked) sediment with an oblate magnetic fabric [56,59].

4.1. Anisotropy of Magnetic Susceptibility for each Cryogenian Series

The robustness of statistical calculations was maintained by limiting calculations to samples of the Cryogenian with $F_{12} > 4$, $\varepsilon_{12} < 22.5°$, and I-$K_{min} > 70°$ (Table 1; Figures 10 and S2). The screened Lower, Middle, and Upper Cryogenian sample sets of each of the eight study outcrops yielded different preferred orientations for the maximum anisotropy of the magnetic susceptibility axis (K_{max}) (modern coordinates; Table 2; Figure 10). In addition, a centroid statistical approach was applied using the Safyr and Anisoft software to assess the distribution of K_{max} values for the screened sample set of each outcrop. In this manner, the dominant orientations were determined. Without considering the inclination, the centroid statistical diagram magnifies variations only in K_{max} declinations (modern coordinates; Tables 2 and 3; Figure 10).

Table 1. The maximum anisotropy of magnetic susceptibility axis (K_{max}) with different preferred orientations and centroid D-K_{max} values for each of the eight study outcrops for each series of the Cryogenian–Ediacaran. Detailed information is given in Figures 10 and 11.

Outcrop	Lower Cryogenian	Middle Cryogenian	Upper Cryogenian	Lower Ediacaran	Upper Ediacaran
QK	(24/46) 52%	(31/51) 61%	(20/48) 41%	(30/49) 61%	(28/45) 62%
SW	(29/44) 65%	(24/52) 46%	(21/48) 43%	(20/44) 45%	(23/48) 47%
TK	(25/49) 51%	(23/55) 41%	(25/54) 46%	(29/46) 62%	(29/52) 55%
XG	(30/51) 58%	(29/53) 54%	(26/49) 53%	(29/57) 50%	(26/50) 52%
XY	(20/46) 44%	(31/57) 55%	(21/52) 41%	(29/53) 55%	(18/46) 40%
XZ	(32/52) 61%	(30/55) 55%	(27/45) 60%	(27/58) 47%	(20/45) 45%
YD	(25/52) 49%	(30/56) 53%	(27/46) 59%	(30/52) 58%	(22/45) 48%
YM	(24/49) 48%	(30/56) 53%	(31/55) 56%	(24/43) 55%	(29/48) 61%

Table 2. The maximum anisotropy of magnetic susceptibility axis (K_{max}) with different preferred orientations and centroid D-K_{max} values for each of the eight study outcrops for each series of the Cryogenian–Ediacaran. Detailed information is given in Figures 10 and 11.

No.	Outcrop	Cryogenian			Ediacaran	
		Lower	Middle	Upper	Lower	Upper
1	QK	256°–1° (centroid 310°)	222°–337° (centroid 280°)	192°–324° (centroid 257°)	166°–301° (centroid 236°)	187°–310° (centroid 249°)
2	SW	248°–4° (centroid 307°)	217°–322° (centroid 273°)	180°–322° (centroid 252°)	177°–294° (centroid 234°)	196°–298° (centroid 249°)
3	TK	257°–356° (centroid 309°)	222°–326° (centroid 275°)	189°–319° (centroid 251°)	166°–314° (centroid 238°)	185°–327° (centroid 260°)
4	XG	243°–6° (centroid 310°)	205°–348° (centroid 278°)	183°–322° (centroid 256°)	171°–308° (centroid 237°)	196°–319° (centroid 258°)
5	XY	251°–352° (centroid 305°)	214°–333° (centroid 276°)	191°–329° (centroid 259°)	174°–302° (centroid 240°)	200°–312° (centroid 256°)
6	XZ	239°–357° (centroid 303°)	199°–351° (centroid 273°)	189°–311° (centroid 253°)	181°–299° (centroid 242°)	203°–307° (centroid 255°)
7	YD	253°–4° (centroid 311°)	215°–345°(centroid 283°)	186°–324° (centroid 258°)	173°–302° (centroid 237°)	194°–313° (centroid 250°)
8	YM	260°–347° (centroid 307°)	202°–350° (centroid 279°)	189°–321° (centroid 261°)	169°–298° (centroid 235°)	183°–321° (centroid 252°)
Mean		308° ± 69°	277° ± 78°	256° ± 76°	237° ± 77°	254° ± 73°

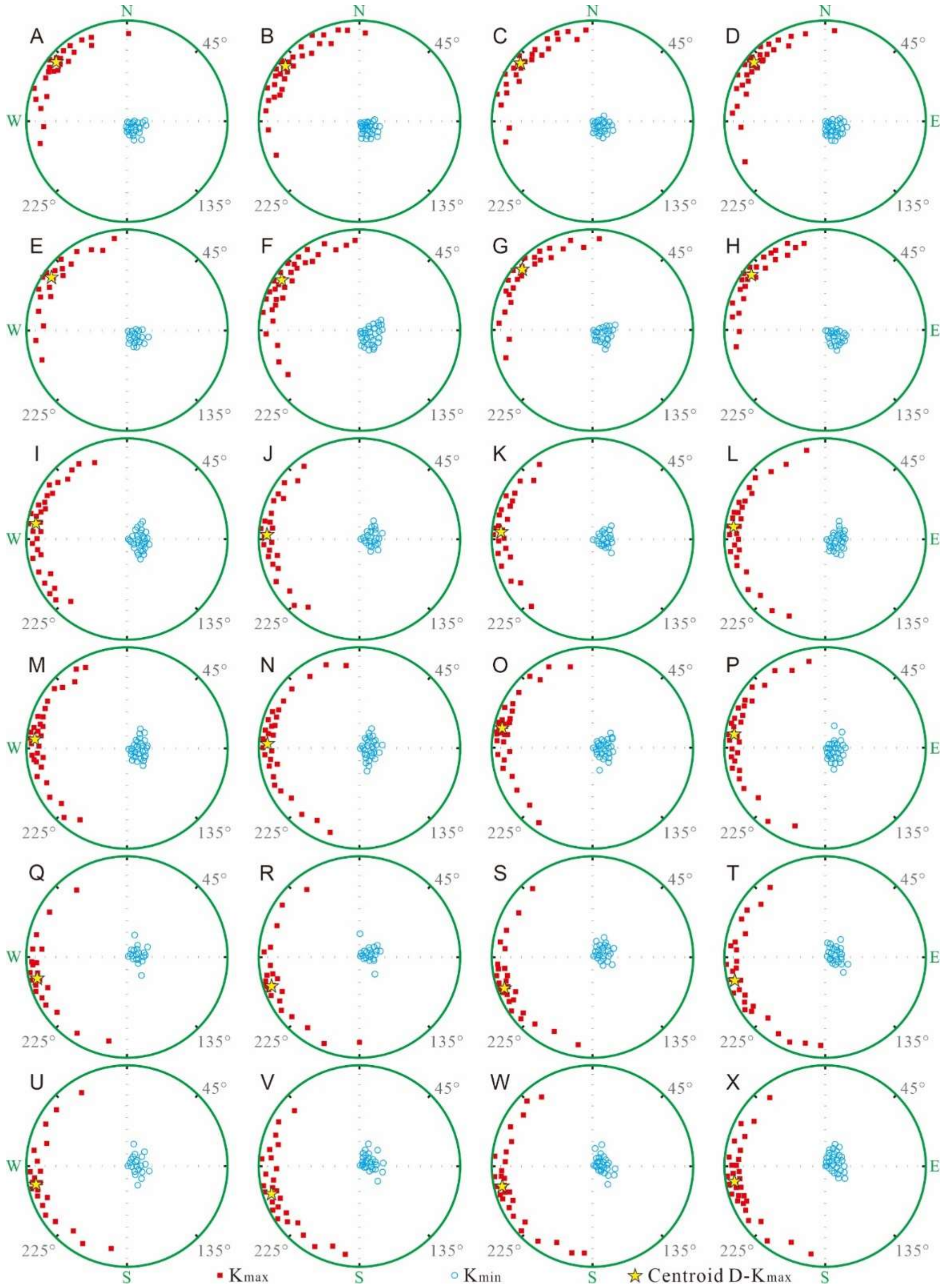

Figure 10. Equal-area projections (modern coordinates) of anisotropy of magnetic susceptibility principal axes of selected samples (according to criteria for which F12 > 4, ε12 < 22.5°, and I-Kmin > 70°) for each Cryogenian series from the eight outcrops. (**A**) Lower Cryogenian at the QK Outcrop (*n* = 24). (**B**) Lower Cryogenian at the SW Outcrop (*n* = 29). (**C**) Lower Cryogenian at the TK Outcrop (*n* = 25). (**D**) Lower Cryogenian at the XG Outcrop (*n* = 30). (**E**) Lower Cryogenian at the XY Outcrop (*n* = 20). (**F**) Lower Cryogenian at the XZ Outcrop (*n* = 32). (**G**) Lower Cryogenian at the YD Outcrop (*n* = 25). (**H**) Lower Cryogenian at the YH Outcrop (*n* = 24). (**I**) Middle Cryogenian at the QK Outcrop (*n* = 31). (**J**) Middle Cryogenian at the SW Outcrop (*n* = 24). (**K**) Middle Cryogenian at the TK Outcrop (*n* = 23). (**L**) Middle Cryogenian at the XG Outcrop (*n* = 29). (**M**) Middle Cryogenian at the XY Outcrop (*n* = 31). (**N**) Middle Cryogenian at the XZ Outcrop (*n* = 30). (**O**) Middle Cryogenian at the YD Outcrop (*n* = 30). (**P**) Middle Cryogenian at the YM Outcrop (*n* = 30). (**Q**) Upper Cryogenian at the QK Outcrop (*n* = 20). (**R**) Upper Cryogenian at the SW Outcrop (*n* = 21). (**S**) Upper Cryogenian at the TK Outcrop (*n* = 25). (**T**) Upper Cryogenian at the XG Outcrop (*n* = 26). (**U**) Upper Cryogenian at the XY Outcrop (*n* = 21). (**V**) Upper Cryogenian at the XZ Outcrop (*n* = 27). (**W**) Upper Cryogenian at the YD

Outcrop (n = 27). (**X**) Upper Cryogenian at the YM Outcrop (n = 31). K_{max}—maximum principal axes of the three-dimensional anisotropy of magnetic susceptibility ellipsoid; K_{min}—minimum principal axes of the three-dimensional anisotropy of magnetic susceptibility ellipsoid; D-K_{max}—declination of maximum principal axes of the three-dimensional anisotropy of magnetic susceptibility ellipsoid.

Table 3. Mean orientations and uncertainty values of the anisotropy of magnetic susceptibility during each series of the Cryogenian–Ediacaran.

No.	System	Series	Outcrops	D-K_{max}	I-K_{max}	D-K_{int}	I-K_{int}	D-K_{min}	I-K_{min}	Uncertainty Values of D-K_{max}
1	Ediacaran	Upper	QK, SW, TK, XG, XY, XZ, YD, and YM	253.6°	14.3°	338.5°	19.4°	63.1°	77.4°	±72.6°
2		Lower		237.4°	15.8°	320.3°	13.3°	56.7°	73.8°	±77.3°
3	Cryogenian	Upper		255.9°	16.4°	338.2°	26.1°	70.9°	72.2°	±75.8°
4		Middle		277.1°	15.6°	12.9°	13.1°	94.9°	74.3°	±77.9°
5		Lower		307.8°	13.2°	34.4°	21.4°	130.1°	78.7°	±68.7°

4.2. *Anisotropy of Magnetic Susceptibility for Each Ediacaran Series*

Statistical robustness was ensured by limiting calculations to Ediacaran samples with $F_{12} > 4$, $\varepsilon_{12} < 22.5°$, and I-$K_{min} > 70°$ (Table 1; Figures 11 and S3). The screened Lower and Upper Ediacaran sample sets of each of the eight study outcrops yielded different preferred orientations for the maximum anisotropy of the magnetic susceptibility axis (K_{max}) (modern coordinates; Table 2; Figure 10). In addition, a centroid statistical approach was applied using the Safyr and Anisoft software to assess the distribution of K_{max} values for the screened sample set of each outcrop. In this manner, the dominant orientations were determined. Without considering the inclination, the centroid statistical diagram magnifies variations only in K_{max} declinations (modern coordinates; Tables 2 and 3; Figure 11).

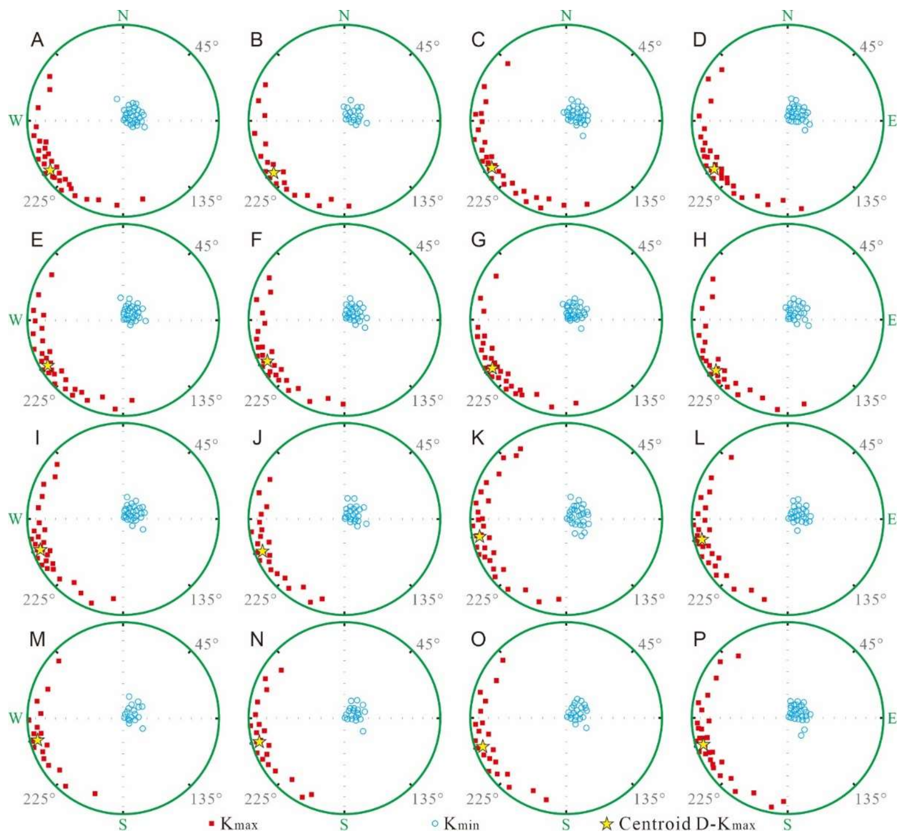

Figure 11. Equal-area projections (modern coordinates) of anisotropy of magnetic susceptibility principal axes of selected samples (according to criteria for which F12 > 4, ε12 < 22.5°, and I-Kmin > 70°) for each

Ediacaran series from the eight outcrops. (**A**) Lower Ediacaran at the QK Outcrop (n = 30). (**B**) Lower Ediacaran at the SW Outcrop (n = 20). (**C**) Lower Ediacaran at the TK Outcrop (n = 29). (**D**) Lower Ediacaran at the XG Outcrop (n = 29). (**E**) Lower Ediacaran at the XY Outcrop (n = 29). (**F**) Lower Ediacaran at the XZ Outcrop (n = 27). (**G**) Lower Ediacaran at the YD Outcrop (n = 30). (**H**) Lower Ediacaran at the YM Outcrop (n = 24). (**I**) Upper Ediacaran at the QK Outcrop (n = 28). (**J**) Upper Ediacaran at the SW Outcrop (n = 23). (**K**) Upper Ediacaran at the TK Outcrop (n = 29). (**L**) Upper Ediacaran at the XG Outcrop (n = 26). (**M**) Upper Ediacaran at the XY Outcrop (n = 18). (**N**) Upper Ediacaran at the XZ Outcrop (n = 20). (**O**) Upper Ediacaran at the YD Outcrop (n = 22). (**P**) Upper Ediacaran at the YM Outcrop (n = 29). K_{max}—maximum principal axes of the three-dimensional anisotropy of magnetic susceptibility ellipsoid; K_{min}—minimum principal axes of the three-dimensional anisotropy of magnetic susceptibility ellipsoid; D-K_{max}—declination of maximum principal axes of the three-dimensional anisotropy of magnetic susceptibility ellipsoid.

5. Discussion

5.1. Reconstruction of Paleowind Directions Quantitatively

The anisotropy of magnetic susceptibility can be used to determine the prevailing paleowind directions [57,59,68,69]. Examples in previous studies include the reconstruction of the route of the paleomonsoon along a west-to-east transect in the Chinese Loess Plateau [57], and the reconstruction of paleowind directions and sources of detrital material archived in the Roxolany loess section, southern Ukraine [59].

The orientations of the anisotropy of magnetic susceptibility of the samples can be explained on the basis of a model of strong unidirectional flow (Figure S1B) [66,68,69], which is the most consistent with the distribution of data in the current study (Figures 10 and 11). Most grains in this model were oriented parallel to unidirectional flow (Figure S1B) [66,68,69]. The paleowind directions in the Early, Middle, and Late Cryogenian were 308° ± 69°, 277° ± 78°, and 256° ± 76°, respectively (modern coordinates; Figure 12A–C). The paleowind directions in the Early and Late Ediacaran were 237° ± 77° and 254° ± 73°, respectively (modern coordinates; Figure 12D,E). The present study proposes an approach for quantitatively reconstructing the paleowind directions of ancient blocks using the anisotropy of magnetic susceptibility.

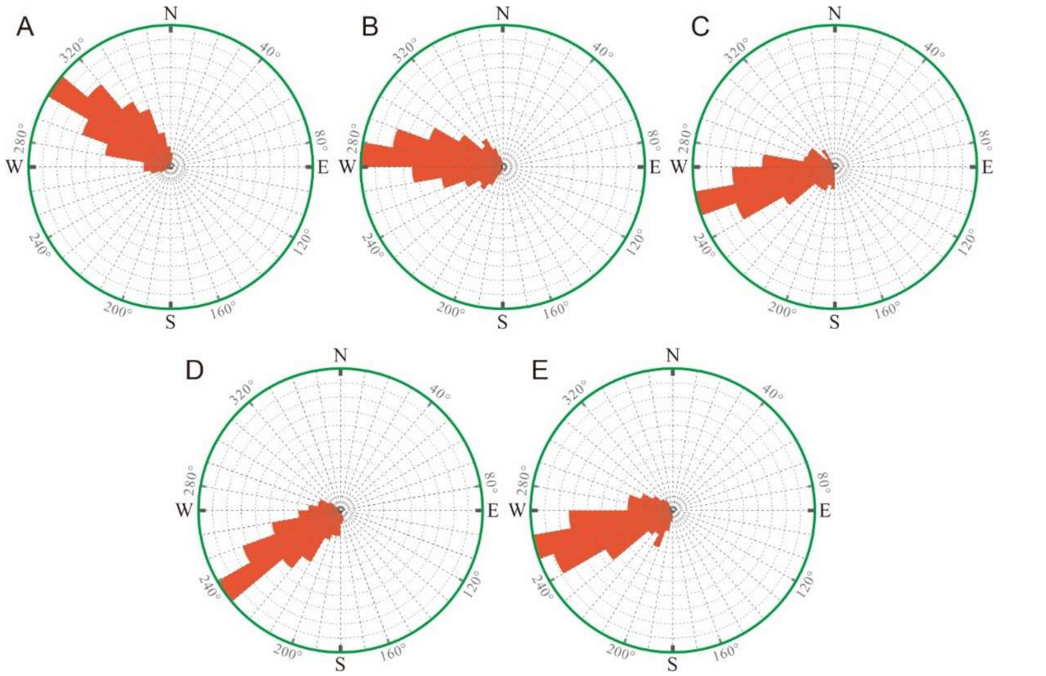

Figure 12. Comprehensively interpretative rose diagram showing the prevailing paleowind directions for each epoch of the Cryogenian–Ediacaran. (**A**) Early Cryogenian. (**B**) Middle Cryogenian. (**C**) Late Cryogenian. (**D**) Early Ediacaran. (**E**) Late Ediacaran.

5.2. Significance of Paleowind Directions for Paleogeography

The prevailing paleowind directions have important paleogeographic implications for the Tarim Block (Figure 13). The Tarim Block was located in the low to middle latitudes during the Cryogenian–Ediacaran [5,23–25] (Figure 1). However, its exact position remains debatable because relevant paleomagnetic data are lacking. Some scholars hold that the Tarim Block was located at about 40° N during the Cryogenian (~750 Ma) and that the northern area was adjacent to the northwest of the Australian Block (modern orientation) (Figure 1A). During the Ediacaran, the Tarim Block shifted southward to about 27° N, with a counterclockwise rotation [23] (Figure 1B). Other scholars believe that the large-scale rotation was at near-constant paleolatitudes during the Cryogenian [24,31,32]. The rotation was coeval with Rodinia breakup, and the paleolatitudes of the Tarim Block are compatible with its placement between Australia and Laurentia [24,31,33] (Figure 1C,D).

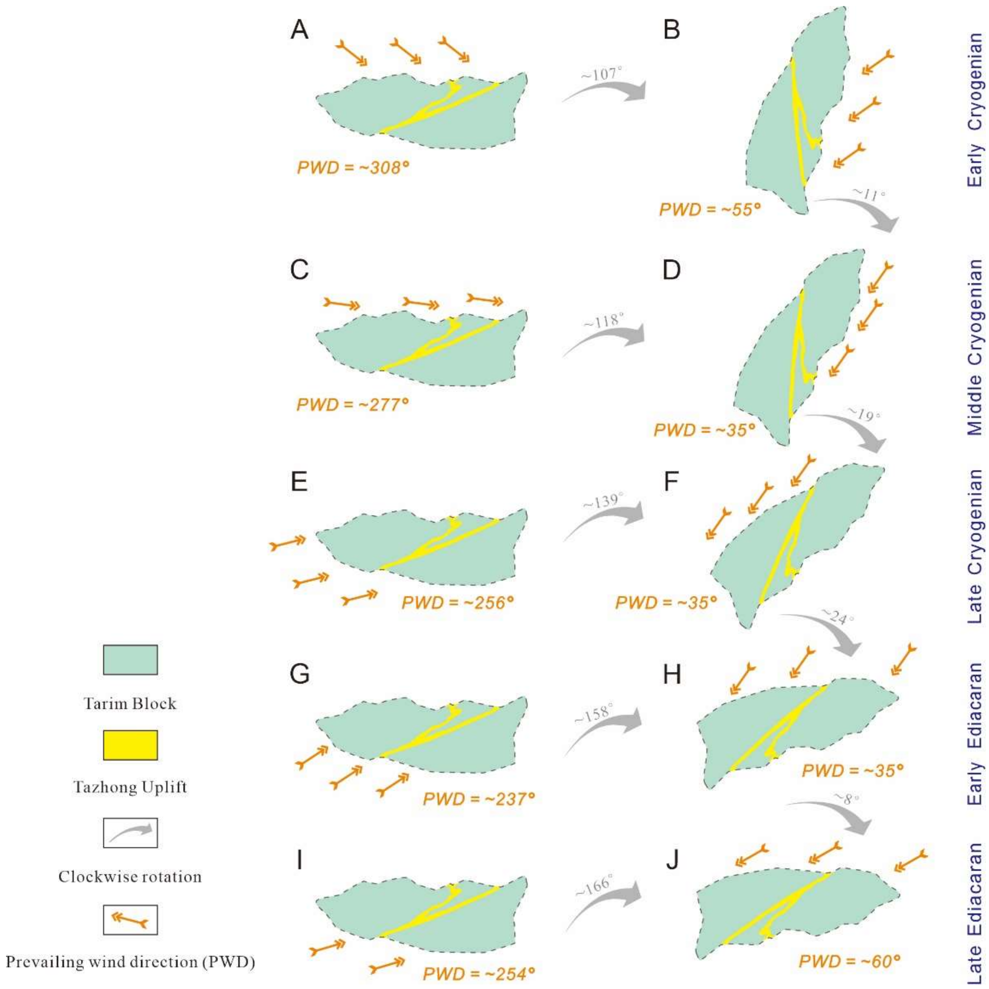

Figure 13. Relationship between present and Cryogenian–Ediacaran geographic orientations of the Tarim Block. Paleowind orientations of the Tarim Block are shown in modern coordinate (left) and paleo-coordinate (right) frameworks. Data are for Early Cryogenian facies (**A**,**B**), Middle Cryogenian facies (**C**,**D**), Late Cryogenian facies (**E**,**F**), Early Ediacaran facies (**G**,**H**), and Late Ediacaran facies (**I**,**J**). The prevailing wind directions for each Cryogenian–Ediacaran series are based on the AMS results from Table 2 and Figures 10 and 11. Syn- and post-Cryogenian and Ediacaran tectonic rotations are shown by tapered gray arrows.

Referring to the current position of the Tarim Block, its paleowind directions would have been 308° ± 69° during the Early Cryogenian, 277° ± 78° during the Middle Cryogenian, 256° ± 76° during the Late Cryogenian, 237° ± 77° during the Early Ediacaran, and 254° ± 73° during the Late Ediacaran (Tables 2 and 3; Figure 12). This conclusion is consistent with the most recent paleogeographic findings (e.g., [24]): (1) During the Early Cryogenian, the Tarim Block was located in the Northern Hemisphere (~10° N), and the prevailing paleowind direction was ~308° (modern coordinates). The plate has rotated ~107° counterclockwise since the Early Cryogenian, indicating a paleowind direction of ~55° in paleo-coordinates (Figure 13A,B). (2) During the Middle Cryogenian, the Tarim Block was located in the Northern Hemisphere (~20° N), and the prevailing paleowind direction was ~277° (modern coordinates). The plate has rotated ~118° counterclockwise since the Middle Cryogenian, indicating a paleowind direction of ~35° in paleo-coordinates (Figure 13C,D). (3) During the Late Cryogenian, the Tarim Block was located in the Northern Hemisphere (~20° N), and the prevailing paleowind direction was ~256° (modern coordinates). The plate has rotated ~139° counterclockwise since the Late Cryogenian, indicating a paleowind direction of ~35° in paleo-coordinates (Figure 13E,F). (4) During the Early Ediacaran, the Tarim Block was located in the Northern Hemisphere (~20° N), and the prevailing paleowind direction was ~237° (modern coordinates). The plate has rotated ~158° counterclockwise since the Early Ediacaran, indicating a paleowind direction of ~35° in paleo-coordinates (Figure 13G,H). (5) During the Late Ediacaran, the Tarim Block was located in the Northern Hemisphere (~7° N), and the prevailing paleowind direction was ~254° (modern coordinates). The plate has rotated ~166° counterclockwise since the Late Ediacaran, indicating a paleowind direction of ~60° in paleo-coordinates (Figure 13I,J) [24,31,33].

The prevailing directions of the trade winds belt slightly vary at different locations. The prevailing wind direction is nearly north (20°–45°) at locations far from the equator in the Northern Hemisphere and nearly east (45°–70°) at locations near the equator in the Northern Hemisphere [70–72]. The Tarim Block was located at ~20° N during the Middle Cryogenian to Early Ediacaran [24,31,33]. The relevant paleowind direction was ~35°, which is between 20° and 45° (paleo-coordinates) (Figure 13D,F,H). The Tarim Block was located at ~10° N and ~7° N during the Early Cryogenian and Late Ediacaran, respectively. The relevant paleowind directions were ~55° and ~60°, which are between 45° and 70° (paleo-coordinates) (Figure 13B,J). This study provides evidence for the paleogeography of the Tarim Block during the Cryogenian–Ediacaran in terms of the prevailing paleowind directions over the Tarim Block and the trade winds in the Northern Hemisphere. The determination of paleowind directions can be of geological significance for ancient blocks. For example, as shown in the present study, the paleogeography of a block can be constrained using paleowind directions.

6. Conclusions

The Tarim Block was located in the low latitude trade wind belt during the Cryogenian–Ediacaran and was affected by the prevailing wind directions. Analysis of the anisotropy of magnetic susceptibility indicated that the paleowind directions over the Tarim Block during the Early, Middle, and Late Cryogenian were 308° ± 69°, 277° ± 78°, and 256° ± 76°, respectively, whereas those during the Early and Late Ediacaran were 237° ± 77° and 254° ± 73°, respectively (modern coordinates). This study quantitatively reconstructed the prevailing paleowind directions over the Tarim Block through an analysis of the anisotropy of magnetic susceptibility. Referring to the corresponding relationship between the prevailing paleowind directions over the Tarim Block and trade winds in the Northern Hemisphere, the findings also provide evidence for the location of the Tarim Block during the Cryogenian–Ediacaran. The results can provide a reference for the study of the paleogeography of the Tarim Block during the Mesoproterozoic.

Supplementary Materials: The following supporting information can be downloaded at: https://www.mdpi.com/article/10.3390/min12111435/s1, Figure S1: Theoretical depositional fabric in the presence of wind or water currents. The orange grains illustrate the preferred alignment of most magnetic particles.; Figure S2.: Equal-area projections (modern coordinates) of anisotropy of magnetic susceptibility principal axes of all samples for each Cryogenian series from the eight outcrops.; Figure S3. Equal-area projections (modern coordinates) of anisotropy of magnetic susceptibility principal axes of all samples for each Ediacaran series from the eight outcrops.; Table S1: Location and sampling information for the eight study outcrops.

Author Contributions: Conceptualization, C.H. (Chenlin Hu) and C.H. (Changcheng Han); methodology, C.H. (Chenlin Hu); software, C.H. (Changcheng Han); validation, J.M., L.D. and L.Z.; formal analysis, C.H. (Chenlin Hu); investigation, J.M., L.D. and L.Z.; resources, C.H. (Chenlin Hu); data curation, C.H. (Changcheng Han); writing—original draft preparation, C.H. (Chenlin Hu); writing—review and editing, C.H. (Changcheng Han); visualization, C.H. (Changcheng Han); supervision, C.H. (Chenlin Hu); project administration, C.H. (Chenlin Hu) and C.H. (Changcheng Han); funding acquisition, C.H. (Chenlin Hu) and C.H. (Changcheng Han). All authors have read and agreed to the published version of the manuscript.

Funding: This research was funded by the Natural Science Foundation of Xinjiang Uygur Autonomous Region, grant numbers 2020D01C064 and 2020D01C037 and the Natural Science Foundation of China, grant number 42062010.

Data Availability Statement: All relevant data used for the research described in this article are included in the article and/or its Supplementary Files. Upon the request to the corresponding author or first author, the data are available.

Acknowledgments: We thank Shiqi Wang, Song Lu, Jing Bian, Rufei Peng, and Yuqing Dong for their help in data analysis. Thanks are also extended to two anonymous reviewers for their constructive comments.

Conflicts of Interest: The authors declare that they have no known competing financial interests or personal relationships that could have appeared to influence the work reported in this paper.

References

1. Gladkochub, D.P.; Donskaya, T.V.; Stanevich, A.M.; Pisarevsky, S.A.; Zhang, S.; Motova, Z.L.; Mazukabzov, A.M.; Li, H. U-Pb detrital zircon geochronology and provenance of Neoproterozoic sedimentary rocks in southern Siberia: New insights into breakup of Rodinia and opening of Paleo-Asian Ocean. *Gondwana Res.* **2019**, *65*, 1–16. [CrossRef]
2. Poprawa, P.; Krzemińska, E.; Pacześna, J.; Amstrong, R. Geochronology of the Volyn volcanic complex at the western slope of the East European Craton–Relevance to the Neoproterozoic rifting and the break-up of Rodinia/Pannotia. *Precambrian Res.* **2020**, *346*, 105817. [CrossRef]
3. Kulakov, E.V.; Slagstad, T.; Ganerød, M.; Torsvik, T.H. Paleomagnetism and 40Ar/39Ar geochronology of Meso-Neoproterozoic rocks from southwest Norway. Implications for magnetic remanence ages and the paleogeography of Baltica in a Rodinia supercontinent context. *Precambrian Res.* **2022**, *379*, 106786. [CrossRef]
4. Zhang, F.-Q.; Dilek, Y.; Cheng, X.-G.; Wu, H.-X.; Lin, X.-B.; Chen, H.-L. Late Neoproterozoic–early Paleozoic seismic structure–stratigraphy of the SW Tarim Block (China), its passive margin evolution and the Tarim–Rodinia breakup. *Precambrian Res.* **2019**, *334*, 105456. [CrossRef]
5. Zhao, P.; He, J.; Deng, C.; Chen, Y.; Mitchell, R.N. Early Neoproterozoic (870–820 Ma) amalgamation of the Tarim craton (northwestern China) and the final assembly of Rodinia. *Geology* **2021**, *49*, 1277–1282. [CrossRef]
6. Wu, H.-X.; Zhang, F.-Q.; Dilek, Y.; Chen, H.-L.; Wang, C.-Y.; Lin, X.-B.; Chen, X.-G.; Zhu, K.-Y. Mid–Neoproterozoic collision of the Tarim Craton with the Yili–Central Tianshan Block towards the final assembly of Supercontinent Rodinia: A new model. *Earth-Sci. Rev.* **2022**, *228*, 103989. [CrossRef]
7. He, J.; Xu, B.; Li, D. Newly discovered early Neoproterozoic (ca. 900 Ma) andesitic rocks in the northwestern Tarim Craton: Implications for the reconstruction of the Rodinia supercontinent. *Precambrian Res.* **2019**, *325*, 55–68. [CrossRef]
8. Ren, R.; Guan, S.-W.; Zhang, S.-C.; Wu, L.; Zhang, H.-Y. How did the peripheral subduction drive the Rodinia breakup: Constraints from the Neoproterozoic tectonic process in the northern Tarim Craton. *Precambrian Res.* **2020**, *339*, 105612. [CrossRef]
9. Zhu, G.-Y.; Chen, Z.-Y.; Chen, W.-Y.; Yan, H.-H.; Zhang, P.-H. Revisiting to the Neoproterozoic tectonic evolution of the Tarim Block, NW China. *Precambrian Res.* **2021**, *352*, 106013. [CrossRef]
10. Wood, R.; Liu, A.G.; Bowyer, F.; Wilby, P.R.; Dunn, F.S.; Kenchington, C.G.; Hoyal Cuthill, J.F.; Mitchell, E.G.; Penny, A. Integrated records of environmental change and evolution challenge the Cambrian Explosion. *Nat. Ecol. Evol.* **2019**, *3*, 528–538.
11. Darroch, S.A.; Cribb, A.T.; Buatois, L.A.; Germs, G.J.; Kenchington, C.G.; Smith, E.F.; Mocke, H.; Neil, G.R.; Schiffbauer, J.D.; Maloney, K.M.; et al. The trace fossil record of the Nama Group, Namibia: Exploring the terminal Ediacaran roots of the Cambrian explosion. *Earth-Sci. Rev.* **2021**, *212*, 103435. [CrossRef]

12. Giuliani, A.; Drysdale, R.N.; Woodhead, J.D.; Planavsky, N.J.; Phillips, D.; Hergt, J.; Griffin, W.L.; Oesch, S.; Dalton, H.; Davies, G.R. Perturbation of the deep-Earth carbon cycle in response to the Cambrian Explosion. *Sci. Adv.* **2022**, *8*, eabj1325. [CrossRef] [PubMed]
13. Gallet, Y.; Pavlov, V.; Korovnikov, I. Extreme geomagnetic reversal frequency during the Middle Cambrian as revealed by the magnetostratigraphy of the Khorbusuonka section (northeastern Siberia). *Earth Planet. Sci. Lett.* **2019**, *528*, 115823. [CrossRef]
14. Sergeev, V.N.; Schopf, J.W.; Kudryavtsev, A.B. Global microfossil changes through the Precambrian-Cambrian phosphogenic event: The Shabakta Formation of the phosphorite-bearing Maly Karatau Range, South Kazakhstan. *Precambrian Res.* **2020**, *349*, 105386. [CrossRef]
15. Tatzel, M.; Stuff, M.; Franz, G.; Hippler, D.; Wiechert, U.; von Blanckenburg, F. Siliceous sponge expansion and phosphogenesis in a shallow water environment in the Malyi Karatau Range (Kazakhstan) during the Precambrian-Cambrian transition. *Precambrian Res.* **2020**, *347*, 105830. [CrossRef]
16. Steadman, J.A.; Large, R.R.; Blamey, N.J.; Mukherjee, I.; Corkrey, R.; Danyushevsky, L.V.; Maslennikov, V.; Hollings, P.; Garven, G.; Brand, U.; et al. Evidence for elevated and variable atmospheric oxygen in the Precambrian. *Precambrian Res.* **2020**, *343*, 105722. [CrossRef]
17. Frederiksen, J.A.; Wei, W.; Rugen, E.J.; Ling, H.F.; Frei, R. Cadmium isotopes in Late Ediacaran–Early Cambrian Yangtze Platform carbonates–Reconstruction of bioproductivity in ambient surface seawater. *Palaeogeogr. Palaeocl.* **2022**, 111096. [CrossRef]
18. Shizuya, A.; Kaiho, K.; Tong, J.N. Marine biomass changes during and after the Neoproterozoic Marinoan global glaciation. *Glob. Planet. Chang.* **2021**, *205*, 103610. [CrossRef]
19. Smith, D.; Palacios-Pérez, M.; Jheeta, S. The Enclosed Intestinal Microbiome: Semiochemical Signals from the Precambrian and Their Disruption by Heavy Metal Pollution. *Life* **2022**, *12*, 287. [CrossRef]
20. Warren, L.V.; Quaglio, F.; Riccomini, C.; Simões, M.G.; Poire, D.G.; Strikis, N.M.; Anelli, L.E.; Strikis, P.C. The puzzle assembled: Ediacaran guide fossil Cloudina reveals an old proto-Gondwana seaway. *Geology* **2014**, *42*, 391–394. [CrossRef]
21. Servais, T.; Perrier, V.; Danelian, T.; Klug, C.; Martin, R.; Munnecke, A.; Nowak, H.; Nutzel, A.; Vandenbroucke, T.R.A.; Williams, M.; et al. The onset of the 'Ordovician Plankton Revolution'in the late Cambrian. *Palaeogeogr. Palaeocl.* **2016**, *458*, 12–28. [CrossRef]
22. Kocsis, Á.T.; Scotese, C.R. Mapping paleocoastlines and continental flooding during the Phanerozoic. *Earth-Sci. Rev.* **2021**, *213*, 103463. [CrossRef]
23. Zhou, X.B.; Li, J.H.; Fu, C.J.; Li, W.S.; Wang, H.H. The Nanhuan-Cambrian tectonic setting and tectono-sedimentary events in the northern margin of Tarim Basin. *Geol. China* **2012**, *39*, 900–911.
24. Wen, B.; Evans, D.A.; Li, Y.-X. Neoproterozoic paleogeography of the Tarim Block: An extended or alternative "missing-link" model for Rodinia? *Earth Planet. Sc. Lett.* **2017**, *458*, 92–106. [CrossRef]
25. Chang, L.; Zhang, S.; Li, H.; Xian, H.; Wu, H.; Yang, T. New paleomagnetic insights into the Neoproterozoic connection between South China and India and their position in Rodinia. *Geophys. Res. Lett.* **2022**, e2022GL098348. [CrossRef]
26. Song, J.; Gong, H.; Yao, J.; Zhao, H.; Zhao, X.; Zhang, Y.; Chen, B. U–Pb Dating and Hf Isotopes Analysis of Detrital Zircons of the Shanxi Formation in the Otuokeqi Area, Northwestern Ordos Basin. *Geofluids* 2021. [CrossRef]
27. Wang, P.; Zhao, G.; Liu, Q.; Han, Y.; Yao, J.; Li, J. Zircons from the Tarim basement provide insights into its positions in Columbia and Rodinia supercontinents. *Precambrian Res.* **2020**, *341*, 105621. [CrossRef]
28. Wu, G.; Yang, S.; Liu, W.; Nance, R.D.; Chen, X.; Wang, Z.; Xiao, Y. Switching from advancing to retreating subduction in the Neoproterozoic Tarim Craton, NW China: Implications for Rodinia breakup. *Geosci. Front.* **2021**, *12*, 161–171. [CrossRef]
29. Andersen, T.; Elburg, M.A.; van Niekerk, H.S.; Ueckermann, H. Successive sedimentary recycling regimes in southwestern Gondwana: Evidence from detrital zircons in Neoproterozoic to Cambrian sedimentary rocks in southern Africa. *Earth-Sci. Rev.* **2018**, *181*, 43–60. [CrossRef]
30. Maitra, A.; Bose, S.; Ghosh, A.; Gupta, S. Neoproterozoic extension and decompression in the northern Eastern Ghats Province, India: Mid-crustal signature of Rodinia break-up? *Precambrian Res.* **2021**, *358*, 106149. [CrossRef]
31. Huang, B.; Xu, B.; Zhang, C.; Li, Y.; Zhu, R. Paleomagnetism of the Baiy-isi volcanic rocks (ca. 740 Ma) of Tarim Northwest China: A continental fragment of Neoproterozoic Western Australia? *Precambrian Res.* **2005**, *142*, 83–92. [CrossRef]
32. Wen, B.; Li, Y.-X.; Zhu, W. Paleomagnetism of the Neoproterozoic diamictites of the Qiaoenbrak formation in the Aksu area, NW China: Constraintson the paleogeographic position of the Tarim Block. *Precambrian Res.* **2013**, *226*, 75–90. [CrossRef]
33. Li, Z.-X.; Evans, D.A.D. Late Neoproterozoic 40 intraplate rotation within Australia allows for a tighter-fitting and longer-lasting Rodinia. *Geology* **2011**, *39*, 39–42. [CrossRef]
34. Shen, W.; Zhu, X.; Xie, H.; Wang, X.; He, Y. Tectonic–sedimentary evolution during initiation of the Tarim Basin: Insights from late Neoproterozoic sedimentary records in the NW basin. *Precambrian Res.* **2022**, *371*, 106598. [CrossRef]
35. Chen, H.; Lin, X.; Cheng, X.; Yang, S.; Zhang, F.; Wu, L.; Ding, W.; Li, Y.; Hu, B.; Huang, W.; et al. The Late Neoproterozoic sedimentary sequences in the Yutang section southwest Tarim Basin and their tectonic implications and hydrocarbon perspective: Insight from basinology. *Precambrian Res.* **2019**, *333*, 105432. [CrossRef]
36. Chen, W.-Y.; Zhu, G.-Y.; Zhang, K.-J.; Zhang, Y.-J.; Yan, H.-H.; Du, D.-D.; Zhang, Z.-Y.; Xia, B. Late Neoproterozoic intracontinental rifting of the Tarim carton, NW China: An integrated geochemical, geochronological and Sr–Nd–Hf isotopic study of siliciclastic rocks and basalts from deep drilling cores. *Gondwana Res.* **2020**, *80*, 142–156. [CrossRef]
37. Zhu, G.; Yan, H.; Chen, W.; Yan, L.; Zhang, K.; Li, T.; Chen, Z.; Wu, G.; Santosh, M. Discovery of Cryogenian interglacial source rocks in the northern Tarim, NW China: Implications for Neoproterozoic paleoclimatic reconstructions and hydrocarbon exploration. *Gondwana Res.* **2020**, *80*, 370–384. [CrossRef]

38. Zhang, Y.; Yang, T.; Hohl, S.V.; Zhu, B.; He, T.; Pan, W.; Chen, Y.; Yao, X.; Jiang, S. Seawater carbon and strontium isotope variations through the late Ediacaran to late Cambrian in the Tarim Basin. *Precambrian Res.* **2020**, *345*, 105769. [CrossRef]
39. Wang, Y.; Chen, D.; Liu, M.; Liu, K.; Tang, P. Ediacaran carbon cycling and Shuram excursion recorded in the Tarim Block, northwestern China. *Precambrian Res.* **2022**, *377*, 106694. [CrossRef]
40. Zhang, Z.; Zhu, G.; Wu, G.; Li, T.; Feng, X.; Jing, Y. Carbon isotopic chemostratigraphy of the Ediacaran-Cambrian successions in the northwestern Tarim Craton, NW China: Correlations with Gondwana supercontinent. *Glob. Planet. Chang.* **2022**, *208*, 103702. [CrossRef]
41. Wu, L.; Guan, S.W.; Yang, H.J.; Ren, R.; Zhu, G.Y.; Jin, J.Q.; Zhang, C.Y. Paleogeographic pattern and hydrocarbon exploration potential of Neoproterozoic rift basin in northern Tarim. *Acta. Petrolei. Sin.* **2017**, *38*, 375–385.
42. Zhou, X.; Tian, W.; Wu, G.; Nance, R.D.; Chen, Y.; Zhao, Y.; Yan, W.; Zhang, Y. Geochemistry and U-Pb-Hf zircon systematics of Cryogenian syn-rift magmatic rocks from the subsurface of the Tarim Craton: Implications for subduction-related continental rifting. *Precambrian Res.* **2022**, *377*, 106733. [CrossRef]
43. He, J.; Qing, H.; Xu, B. The unconformity-related palaeokarst in the uppermost Ediacaran carbonate rocks in the northwestern Tarim Block, NW China: Implication for sedimentary evolution during the Ediacaran–Cambrian transition. *Int. Geol. Rev.* **2019**, *61*, 839–852. [CrossRef]
44. Ma, B.; Tian, W.; Wu, G.; Nance, R.D.; Zhao, Y.; Chen, Y.; Huang, S. The subduction-related the Great Unconformity in the Tarim intracraton, NW China. *Glob. Planet. Chang.* **2022**, *215*, 103883. [CrossRef]
45. Jiang, L.; Worden, R.; Cai, C.; Shen, A.; Crowley, S. Diagenesis of an evaporiterela-ted carbonate reservoir in deeply buried Cambrian strata, Tarim Basin, Northwest China. *AAPG Bull.* **2018**, *102*, 77–102.
46. Li, P.W.; Luo, P.; Chen, M.; Song, J.M.; Jin, T.F.; Wang, G.Q. Characteristics and genesis of microbial carbonate reservoirs in the Upper Sinian in the northwestern margin of Tarim Basin. *Oil Gas Geol.* **2015**, *36*, 416–428.
47. Shi, K.B.; Liu, B.; Jiang, W.M.; Luo, Q.Q.; Gao, X.Q. Nanhuan-sinian tectonic-sedimentary pattern in Tarim Basin. *Oil Gas Geol.* **2018**, *39*, 862–877.
48. Zhu, G.; Yan, H.; Chen, W.; Yan, L.; Chen, Z.; Li, T.; Sun, Q.; Xie, X. Geochemical characteristics, formation and distribution of Nanhuan-Cambrian black rock series in eastern Tarim Basin. *Acta Petrol. Sin.* **2020**, *36*, 3442–3462.
49. Cohen, K.M.; Finney, S.C.; Gibbard, P.L.; Fan, J.-X. The ICS international chronostratigraphic chart. *Episodes* **2013**, *36*, 199–204.
50. Shi, K.B.; Liu, B.; Liu, H.G.; Liu, J.Q.; Pan, W.Q. Neoproterozoic tectono-sedimentary evolution of Kuluktag area, northeastern margin of Tarim Basin. *Earth Sci. Front.* **2017**, *24*, 297–307.
51. Ren, R.; Guan, S.; Wu, L.; Zhu, G. Evolution of the Neoproterozoic rift basins and its implication for oil and gas exploration in the Tarim Basin. *Petroleum Res.* **2018**, *3*, 66–76. [CrossRef]
52. Wu, H.-X.; Dilek, Y.; Zhang, F.-Q.; Chen, H.-L.; Chen, H.; Wang, C.-Y.; Lin, X.-B.; Cheng, X.-G. Ediacaran magmatism and rifting along the northern margin of the Tarim craton: Implications for the late Neoproterozoic Rodinia configuration and breakup. *Geol. Soc. Am. Bull.* 2022. [CrossRef]
53. Du, J.; Pan, W. Accumulation conditions and play targets of oil and gas in the Cambrian subsalt dolomite, Tarim Basin, NW China. *Petrol. Explor. Dev.* **2016**, *43*, 360–374. [CrossRef]
54. Dai, B.; Wu, N.; Wang, J.; Bian, L. Analysis of sedimentary environment of Cambrian Yuertusi source rock in keping uplift, tarim basin, China. *Fresen. Environ. Bull.* **2020**, *29*, 8294301.
55. Wei, G.; Zhu, Y.; Zheng, J.; Yu, G.; Ni, X.; Yan, L.; Tian, L.; Huang, L. Tectonic-lithofacies paleogeography, large-scale source-reservoir distribution and exploration zones of Cambrian subsalt formation, Tarim Basin, NW China. *Petrol. Explor. Dev.* **2021**, *48*, 1289–1303. [CrossRef]
56. Lagroix, F.; Banerjee, S.K. The regional and temporal significance of primary aeolian mag-netic fabrics preserved in Alaskan loess. *Earth Planet. Sci. Lett.* **2004**, *225*, 379–395. [CrossRef]
57. Zhang, R.; Kravchinsky, V.A.; Zhu, R.; Yue, L. Paleomonsoon route reconstruction along a W–E transect in the Chinese Loess Plateau using the anisotropy of magnetic susceptibility: Summer monsoon model. *Earth Planet. Sci. Lett.* **2010**, *299*, 436–446. [CrossRef]
58. Zhu, R.; Liu, Q.; Jackson, M.J. Paleoenvironmental significance of the magnetic fab-rics in Chinese loess-paleosols since the last interglacial (<130 ka). *Earth Planet. Sci. Lett.* **2004**, *221*, 55–69.
59. Nawrocki, J.; Gozhik, P.; Lanczont, M.; Panczyk, M.; Komar, M.; Bogucki, A.; Williams, I.S.; Czupyt, Z. Palaeowind directions and sources of detrital material archived in the Rox-olany loess section (southern Ukraine). *Palaeogeogr. Palaeocl.* **2018**, *496*, 121–135. [CrossRef]
60. Jelinek, V. Characterization of the magnetic fabric of rocks. *Tectonophysics* **1981**, *79*, T63–T67. [CrossRef]
61. Gong, H.; Zhang, R.; Yue, L.; Zhang, Y.X.; Li, J. Magnetic fabric from Red clay sediments in the Chinese Loess Plateau. *Sci. Rep.-UK* **2015**, *5*, 1–6. [CrossRef] [PubMed]
62. Constable, C.; Tauxe, L. The bootstrap for magnetic susceptibility tensors. *J. Geophys. Res.-Solid Earth* **1990**, *95*, 8383–8395. [CrossRef]
63. Lagroix, F.; Banerjee, S.K. Paleowind directions from the magnetic fabric of loess profiles in central Alaska. *Earth Planet. Sci. Lett.* **2002**, *195*, 99–112. [CrossRef]
64. Hu, C.; Zhang, Y.; Jiang, Z.; Wang, M.; Han, C. Development of large-scale sand bodies in a fault-bounded lake basin: Pleistocene-Holocene Poyang Lake, Southern China. *J. Paleollimnol.* **2021**, *65*, 407–428. [CrossRef]

65. Rees, A.I.; Woodall, W.A. The magnetic fabric of some laboratory-deposited sediments. *Earth Planet. Sci. Lett.* **1975**, *25*, 121–130. [CrossRef]
66. Tarling, D.H.; Hrouda, F. *The Magnetic Anisotropy of Rocks*; Chapman and Hall: London, UK, 1993; p. 220.
67. Hu, C.; Zhang, Y.; Feng, D.; Wang, M.; Jiang, Z.; Jiao, C. Flume tank simulation on depositional mechanism and controlling factors of beach-bar reservoirs. *J. Earth Sci.-China* **2017**, *28*, 1153–1162. [CrossRef]
68. Hu, C.; Zhang, Y.; Jiang, Z.; Wang, M.; Han, C.; Algeo, T.J. Tectonic and paleogeographic controls on development of the Early–Middle Ordovician Shanganning carbonate platform, Ordos Basin, North China. *AAPG Bull.* **2020**, *104*, 565–593. [CrossRef]
69. Hu, C.; Zhang, Y.; Tian, J.; Wang, W.; Han, C.; Wang, H.; Li, X.; Feng, S.; Han, C.; Algeo, T.J. Influence of paleo-Trade Winds on facies patterns of the Cambrian Shanganning carbonate platform, North China. *Palaeogeogr. Palaeocl.* **2020**, *552*, 109556. [CrossRef]
70. Kajtar, J.B.; Santoso, A.; McGregor, S.; England, M.H.; Baillie, Z. Model under-representation of decadal Pacific trade wind trends and its link to tropical Atlantic bias. *Clim. Dynam.* **2018**, *50*, 1471–1484. [CrossRef]
71. Helfer, K.C.; Nuijens, L.; De Roode, S.R.; Siebesma, A.P. How wind shear affects trade-wind cumulus convection. *J. Adv. Model. Earth Syst.* **2020**, *12*, e2020MS002183. [CrossRef]
72. Helfer, K.C.; Nuijens, L.; Dixit, V.V. The role of shallow convection in the momentum budget of the trades from large-eddy-simulation hindcasts. *Q. J. Roy. Meteor. Soc.* **2021**, *147*, 2490–2505. [CrossRef]